International Journal of Nanomedicine

Dovepress
Taylor & Francis Group

Open Access Full Text Article

ORIGINAL RESEARCH

Precise Control of the in vivo Fate of Nanomicelles Efficiently Treats Advanced Rheumatoid Arthritis via EGFR/JNK/MMP9 Pathway

Na Jia[1], Yunzhen Gao[2], Lan Yang[3], Yani Xu[2], Zhirong Zhang[2], Jingwen Wang[1], Ling Zhang[3,4]

[1]Department of Pharmacy, Xijing Hospital, The Fourth Military Medical University, Xi'an, 710032, People's Republic of China; [2]Key Laboratory of Drug Targeting and Drug Delivery Systems, Ministry of Education, West China School of Pharmacy, Chengdu, 610041, People's Republic of China; [3]State Key Laboratory of Polymer Materials Engineering, College of Polymer Science and Engineering, Sichuan University, Chengdu, 610041, People's Republic of China; [4]West China School of Public Health and West China Fourth Hospital, Sichuan University, Chengdu, 610041, People's Republic of China

Correspondence: Jingwen Wang, The Fourth Military Medical University, No. 127 Changle West Road, Xi'an, 710032, People's Republic of China, Email wangjingwen8021@163.com; Ling Zhang, Sichuan University, No. 24 South Section 1, Yihuan Road, Chengdu, 610065, People's Republic of China, Email zhangling83@scu.edu.cn

Purpose: Förster resonance energy transfer (FRET) technology is a tool for in vivo nanomedicine tracking. Nanomicelle-based drug carriers could improve therapeutic outcome for rheumatoid arthritis (RA). Self-assembled nanomicelles are a major type of them, and their drug-loading stability is seriously affected by the in vivo environment. Therefore, it is critical to understand the status of nanomicelles in vivo at different time points, in order to enable precise control of their dynamics to effectively deliver the drug to inflammatory joint.

Methods: We applied FRET technology to elucidate the biofate of nanomicelles in an adjuvant induced arthritis (AIA) mice model and inflammatory larvae zebrafish models. We explored the molecular mechanism of swertiamarin-loaded nanomicelles (SWE-NMs) in improving RA symptoms through network pharmacology, molecular docking and immunofluorescence experiments.

Results: Results showed that on cellular level the nanomicelles could enter inflammatory cells and completely release most cargoes in 12 h, while in animals, the majority of nanomicelles was destroyed within 72 h. Hence, we tailored an administration scheme for RA treatment. As expected, we loaded swertiamarin into the nanomicelles (SWE-NMs). The injection every 3 days (SWE-NMs/3) displayed enhanced accumulation in arthritic joints and strong anti-RA therapeutic effect, as well as good safety profile. In addition, network pharmacology, molecular docking analysis and immunofluorescence experiments revealed that SWE-NMs might work by blocking the epidermal growth factor receptor/c-Jun N-terminal kinase/matrix metalloproteinase (EGFR/JNK/MMP9) pathway.

Conclusion: In summary, this study elucidated the biofate of nanomicelles with FRET technology in RA treatment, thus providing a basis for rationally improving administration scheme and giving clue for investigating other nano delivery systems.

Keywords: nanomicelles, in vivo fate, Swertimarin, Förster resonance energy transfer, efficient treatment, advanced rheumatoid arthritis

Introduction

Nanomicelles targeting rheumatoid arthritis (RA) may enhance the accumulation in targeted inflammatory sites and reduce adverse reactions.[1,2] Micelles are in thermodynamic and kinetic equilibrium with their amphiphilic unimers.[3] Upon entering the blood, the micelles are quickly diluted and mixed with other components in the blood, destroying the micelle structure and releasing drugs.[4,5] In fact, the integrity of micelles in vivo has drawn much attention in recent decades as a basic and important subject. Ideally, the micelles should release drugs after internalizing into cells. However, micelles often dissociate before cell entry, thereby releasing their carrier outside the cell.[6] This inevitably raises two

Received: 10 December 2024
Accepted: 16 April 2025
Published: 25 April 2025

Graphical Abstract

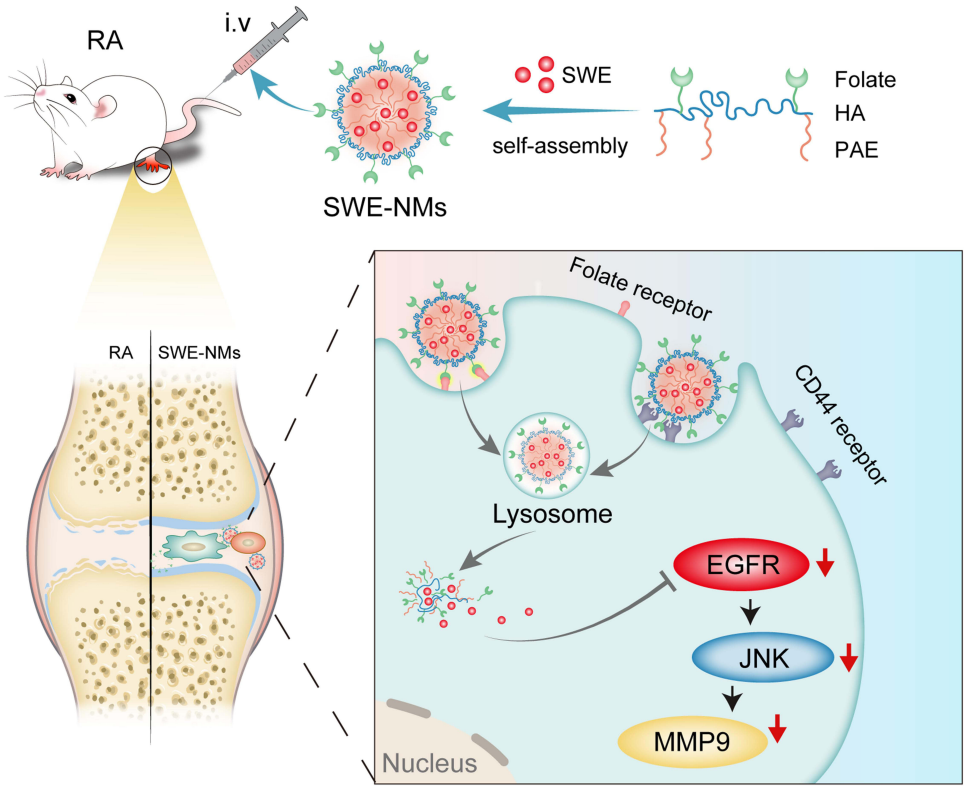

questions: what is the rate and degree of dissociation of micelles once they were injected intravenously into body? Does the drug release prematurely before the micelles reach the target sites, thereby affecting therapeutic efficacy? Clarifying the biofate of nanomicelles in vivo is thus important to answer these questions and provide basis to design nanomicelles and to plan proper administration schemes. In a previous study, we synthesized folate-hyaluronic acid-poly β-amino ester (FA-HA-PAE, Figure 1A) copolymer and constructed a pH-responsive inflammatory targeted nanomicelle delivery system in the rat model of RA.[7] However, its biofate in vivo had not yet been elucidated.

Therefore, it is essential to develop a simple and reliable method to visualize the drug release process of micelles in real time. Förster resonance energy transfer (FRET) dye pairs can partly solve this problem, which lights up only when two dyes locate close enough (<10 nm).[8,9] Chen et al physically embedded a FRET fluorophore pair (3,3′-dioctadecyloxacarbocyanine perchlorate and 1.1′-dioctadecyl-3,3,3′,3′-tetramethylindocarbocyanine perchlorate, DiO and Dil) into small-sized methoxypolyethylene glycols-poly(lactic-co-glycolic acid) (mPEG-PLGA) nanoparticles to track in vivo micellar integrity in zebrafish model.[10] Hsiao et al used FRET pairs (fluorescein isothiocyanate (FITC) and rhodamine B) to assess the stability and bio-distribution of polyethylene oxide-polyphenylene oxide-polyethylene oxide (PEO-PPO-PEO) polymeric micelles in vitro and in vivo on the cornea.[11] In this study, we co-loaded DiD (1,1′-dioctadecyl-3,3,3′,3′-tetramethylindodicarbocyanine,4-chlorobenzenesulfonate; Ex: 640 nm; Em: 660 nm, donor) (Figure 1B) and DiR (1,1′-dioctadecyltetramethyl indotricarbocyanine; Ex: 730 nm; Em: 780 nm, acceptor) into nanomicelles as the FRET pair to study the integrity of micelles.[12] Under this condition, a FRET signal would clearly demonstrate that both fluorophores are present within the same nanoparticle, whereas a FRET signal loss would indicate the release of the dyes from the nanoparticles or breakdown of the micelles.[13]

To effectively guide the treatment of RA consistent with biofate results, we hitchhike the nanomicelles with swertiamarin (SWE, Figure 1C), a functional ingredient from Chinese herb *Gentiana macrophylla* Pall. SWE is an

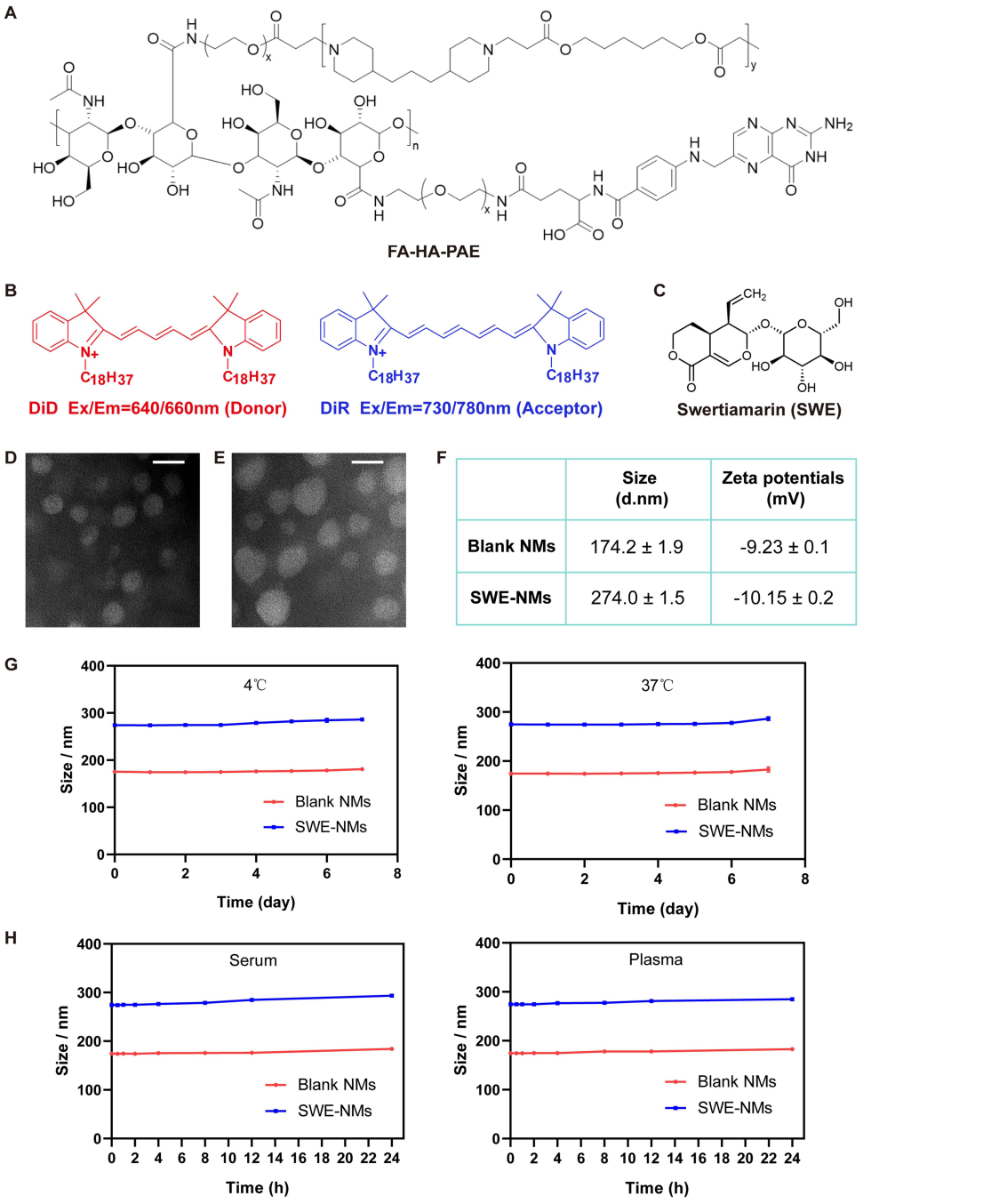

Figure 1 Characterization and stability of SWE-NMs. (**A**) Chemical structures of Folate-Hyaluronic acid-β-amino ester (FA-HA-PAE). (**B**) Chemical structures of the Donor (DiD) and Acceptor (DiR). (**C**) Chemical structures of swertiamarin (SWE). TEM images showed that the blank NMs (**D**) and SWE-NMs (**E**) were roughly spherical with uniformed size. Scale bar = 100 μm. (**F**) The particle sizes of blank NMs and SWE-NMs were about 174.2 nm and 274.0 nm as measured by DLS. The zeta potentials of blank NPs and RBA-NPs were −9.23 mV and −10.15 mV, respectively. (**G**) Stability of SWE-NMs at different temperature (4 or 37°C) in 7 days. (**H**) Stability of SWE-NMs in different conditions (serum or plasma) in 24h at 37°C.

iridoid glycoside proven to treat a variety of diseases, such as diabetes,[14] pulmonary fibrosis,[15] arthritis bone erosion,[16] neurodegenerative disease,[17] and intestinal diseases.[18] Although SWE has significant pharmacological activities, the therapeutic effect is limited due to its poor solubility in water and lack of targeting and accumulation to the inflammatory site of RA. Thus, we chose SWE as the model drug as adequate nanomicelle carriers may significantly improve its therapeutic outcome.

https://doi.org/10.2147/IJN.S511421

So far the molecular target of SWE is not yet clear. Systematic pharmacology is an effective tool for drug-target analysis, which offers low cost, rapidity, and more comprehensive information.[19] This study combined network pharmacology, molecular docking analysis, and experimental verification to explore the molecular mechanism of SWE treatment for RA. Through screening and verification, we first revealed that swertiamarin-loaded nanomicelles (SWE-NMs) might improve RA symptoms by blocking the epidermal growth factor receptor (EGFR)/c-Jun N-terminal kinase (JNK)/matrix metalloproteinase (MMP9) pathway. As a transmembrane receptor tyrosine kinase, EGFR was one of the important receptors for synovial fibroblast proliferation in RA.[20] Meanwhile, EGFR and its ligands induced cytokine production of synovial fibroblasts during the pathogenesis of RA.[21] Matrix metalloproteinases (MMPs), which served as important mediators for extracellular matrix (ECM) degradation and remodeling, played a pivotal role in the progression of RA.[22,23] Previous studies had proved that Ankyrin repeat domain 49 promoted the metastasis of NSCLC via activating JNK-MMP-2/9 axis.[24] MAPK family (ERK, p38, JNK) was closely involved in the abnormal release and activation of RA inflammatory mediators, bone erosion, and cartilage destruction.[25]

In this paper, we used in vitro and in vivo optical imaging studies on adjuvant induced arthritis (AIA) mice model and inflammatory larvae zebrafish models to explore the biofate of functional micelles based on FRET effects. Based on these results, we simply adjusted the administration mode of SWE-NMs in AIA mice with advanced rheumatoid arthritis (advanced RA), which both improved treatment outcomes and ensured safety. At last, possible targets of SWE-NMs for RA were screened through network pharmacology and molecular docking analysis, and its molecular mechanism of RA therapy was explored by in vitro experiments.

Material and Methods

Preparation and Characterization of SWE-NMs

FA-HA-PAE copolymer was synthesized mainly by Michael-addition polymerization and amidate reaction as previously reported. The FA-HA-PAE polymer self-assembled into micelles. Two-milligram SWE and 6 mg FA-HA-PAE copolymer (SWE/FA-HA-PAE copolymer=1/3, w:w) were dissolved in 3 mL of Dimethyl Sulfoxide (DMSO) and 18 mL of deionized water. The SWE-NMs were obtained by emulsifying the mixture with 200W in 10 minutes using a probe-type ultrasonic generator (Scientz, Ningbo, China). The SWE-NMs was placed in a dialysis bag (MWCO = 7000 Da) for dialysis in 48 hours in order to remove free drugs and excess organic solvents. The drug loading (DL) and entrapment efficiency (EE) were surveyed using the following equations:[7]

$$\mathrm{DL}(\%)=\frac{\text{weight of the loaded drug}}{\text{total weight of the drug and the polymer}}\times 100\%$$

$$\mathrm{EE}(\%)=\frac{\text{weight of the loaded drug}}{\text{weight of the drug in the feed}}\times 100\%$$

The particle sizes and zeta potentials of blank NMs and SWE-NMs were characterized by dynamic light scattering (DLS) (Malvern ZetaSizer Nano ZS90, UK). Meanwhile, their morphologies were got by transmission electron microscopy (TEM) (H-600, Hitachi, Japan). The SWE content was detected using UV-vis spectrophotometer (Lambda 365, PerkinElmer, USA) with full wavelength scanning and a maximum absorption wavelength of 235 nm. In the case of DiD/DiR-NMs, the lipophilic dye DiD and DiR were used in place of SWE. About 20 μg DiD, 20 μg DiR, and 5 mg PEG-PAE copolymer were dissolved in 5 mL of anhydrous ethanol. The organic solvent was removed by rotary evaporation at 80 °C.

Fluorescence Spectra

The fluorescence spectra of FRET micelles were measured using a fluorescence spectrometer (Lambda 365, PerkinElmer, USA) at an excitation wavelength of 640 nm with a slit width of 2 nm, integration time of 0.1 s, and increment of 0.5 nm. Emission spectra were collected from 500 to 900 nm.

Cell Culture and Treatments

The murine RAW264.7 cell line was purchased from the American Type Culture Collection (ATCC, USA). RAW264.7 cells were cultured with Dulbecco's modified Eagle's medium (DMEM) supplemented with 10% fetal bovine serum (GIBCO, USA) and 1% penicillin–streptomycin solution in an incubator with 5% CO_2 at 37 °C. After reaching 70–80% confluence, the cells were washed with phosphate buffered saline (PBS) twice and treated with lipopolysaccharide (LPS) (100 ng/mL) and interferon-γ (IFN-γ) (20 ng/mL) for 24h. After that, the cell culture media were changed with 1 mL of fresh media containing DiD/DiR-NMs at a PEG-PAE concentration of 5 μg/mL. After the predetermined time points incubation (0.5, 6, 12h), cells were washed 3 times by PBS. Cells were fixed and stained with DAPI and then photographed by confocal laser scanning microscope (CLSM 800, Zeiss, Germany).

AIA Model

Healthy male BALB/c mice (18–22g, 6 weeks old) were purchased from Chengdu Dashuo Experimental Animal Co., Ltd. (Chengdu, China). Murine were kept in a room with controlled temperature (24±2 °C) and humidity (55%) with free access to food and water. The animal experiments in this study were conducted in line with China's national statute regarding the experimental animals and were approved by Sichuan University's Institutional Animal Care and Ethics Committee. The base of tails in mice were injected subcutaneously with Complete Freund's adjuvant (20 μL) (Chondrex, #7027, Washington DC, USA). The development of arthritis progression was tracked on a daily basis and was fully established at 14 days after injection.

In vivo FRET Imaging in AIA Mice

In vivo fluorescence imaging was performed with an IVIS Spectrum imaging system (Xenogen, Alameda, CA). Images were recorded in DiD channel (640 nm excitation, 660 nm emission) and FRET channel (640 nm excitation, 780 nm emission). The exposure time was 1 s for all of the channels. Identical illumination settings were used for acquiring all images. Images were acquired and analyzed using Living Image 2.5 software (Xenogen, Alameda, CA). The average fluorescence intensities were calculated using the automatic ROI (region of interest) tool of Living Image 2.5 software. The FRET ratio was used to reveal the integrity of FRET nanomicelles by calculating formula: FRET ratio $=I_{DiR}/(I_{DiD} + I_{DiR})$, where I_{DiD} and I_{FRET} mean the fluorescence intensity of the donor (DiD) at 660 nm and acceptor (DiR) at 780 nm under 640 nm excitation, respectively.

In vivo Integrity in Blood of Rats

Healthy male Sprague-Dawley rats (180–220g) were purchased from Chengdu Dashuo Experimental Animal Co., Ltd. (Chengdu, China). The animal experiments in this study were conducted in line with China's national statute regarding the experimental animals and were approved by Sichuan University's Institutional Animal Care and Ethics Committee. The rats were anesthetized at 5 min, 0.5, 1, 2, 4, 6, 12, 24, 48 and 72 h following drug administration. At designated times, the blood samples were collected by enucleation of the rat eyes. The fluorescence intensity was measured by a fluorescence spectrometer at an excitation wavelength of 640 nm with a slit width of 2 nm, integration time of 0.1 s, and increment of 0.5 nm. Emission spectra were collected from 500 to 900 nm.

In vivo FRET Imaging in Larval Zebrafish

Briefly, wildtype larval zebrafish was raised synchronously at 28.5°C in embryo medium (13.7 mm NaCl, 540 μM KCl, 25 μM Na_2HPO_4, 44 μM KH_2PO_4, 300 μM $CaCl_2$, 100 μM $MgSO_4$, 420 μM $NaHCO_3$, pH 7.4). The animal experiments in this study were conducted in line with China's national statute regarding the experimental animals and were approved by Sichuan University's Institutional Animal Care and Ethics Committee. Three days postfertilization (dpf), larval zebrafish were stimulated with LPS (10 μg/mL) for 24 h at 28.5°C and then were transferred into a fresh embryo medium. The LPS concentrations were selected based on a pre-screen for the effective range with up to 10 μg/mL and were well below toxicity in zebrafish embryos. In vivo FRET imaging, DiD/DiR-NMs at a FA-HA-PAE concentration of 20 μg/mL was added to the embryo medium of LPS-treated larval zebrafish. After treatment for 0.5, 6, 24 and 48h, the

embryo medium was replaced with fresh embryo medium, respectively. At the predetermined time points, larval zebrafish were collected and fixed with 4% buffered paraformaldehyde and then imaged by CLSM. Images were recorded in the DiD channel (640 nm excitation, 660 nm emission) and FRET channel (640 nm excitation, 780 nm emission).

Histopathological Examination

Twenty-eight days after arthritis induction, all mice were euthanized. Remove the ankle joint and fix it with 4% paraformaldehyde. Fix the ankle joint with 15% tetrasodium ethylenediaminetetraacetic acid decalcification for 2 months. After the paraffin embedding treatment, cut the slices into 3 pieces μm thick, then stained with hematoxylin-eosin (HE), Safranin-O Fast-Green and toluidine blue. A light microscope (Olympus BX53, Tokyo, Japan) was used to observe staining.

Micro-Computed Tomography (Micro-CT) Imaging

The claws and joints were scanned, and then they were reconstructed into a 3D image using a Siemens Inveon Micro-CT system (Siemens AG, Munich, Germany). At 80 kV voltage, 500 μA current and 750 ms exposure time, the high-resolution scanning method on the micro-CT unit was used for image acquisition. Using software available on the scanner console, a central sagittal cross-section was generated from each set of mouse ankle bone images for analysis. MATERIALISE_MIMICS_V8.1 software was used for defect measurement. Quantitative micro-CT analyses of bone mineral density (BMD) and bone surface density (BS/BV) of the ankle joints were recorded at the endpoint of the experiment for analyzing the level of bone changes.

Immunohistochemical Analysis

Fix the ankle joints of mice after execution with paraformaldehyde (4%). The fixed ankle joint was then decalcified with 15% ethylene diamine tetraacetic acid (EDTA) tetrasodium solution and 15% (w/v) EDTA tetrasodium solution daily for 2 months. Decalcified joints were subsequently embedded in paraffin and stained with sections. The streptavidin-biotin complex (SABC) kit was used for immunolocalization of HIF1α antibody (Affinity, AF1009, 1:100) in the joints.

Assessment of Efficacy

The normal group were injected with an equal volume of physiological saline in the same manner. Methotrexate (MTX) was selected as the positive drug control group. AIA Mice were divided into four groups (n = 5 per group), a model group, MTX (2 mg/kg), two SWE-NMs-treated groups with different administration intervals: low-frequency administration of every 4 days (SWE-NMs/4, dose of 100 mg/kg for SWE) and high-frequency administration of every 3 days (SWE-NMs/3, dose of 100 mg/kg for SWE) with intravenous administration. After arthritis induction, the SWE-NMs/3 group was treated on days 14, 17, 20, 23, and 26, while the SWE-NMs/4 group was treated on days 14, 18, 22, and 26. The arthritis score of mice in each group was assessed every 3 days during treatment. On day 14, each hind limb was scored on a scale of 0 to 4: 0 represents normal; 1 represents mild erythema and/or swelling; 2 represents moderate redness and swelling; 3 represents severe swelling; 4 represents rigidity and inability to withstand weight. The limb scores of each mouse were added together to give a maximum of 16 points. On day 28, the mice were sacrificed via anesthesia (pentobarbital sodium, 65 mg/kg, intraperitoneally). The ankle joint was immediately removed and measured for thickness. The ankle joints of each group mice were immediately removed, and the thickness was measured.

Extracellular Acidification Rate (ECAR)

Cells are prepared in a 96-well plate at a density of 3–8 × 10^4 cells/well in 200 μL culture medium. Cells are incubated overnight in a CO_2 incubator at 37°C. Where cells are cultured in CO_2 incubator overnight, it is important to purge the media and plasticware of CO_2 prior to conducting the assay as residual CO_2 may contribute to acidification. Perform a CO_2 purge by incubating cells in a CO_2-free incubator at 37°C with 95% humidity, approx. 3 hours prior to performing the Glycolysis assay measurement. Remove spent culture media from all assay wells and wash cells with 100 μL of Respiration Buffer. Repeat washing step. Add 150 μL of Respiration Buffer to all wells containing cells. Blank controls: add 150 μL of Respiration Buffer. Add 10 μL reconstituted Glycolysis Assay Reagent to each sample well and positive/negative control wells. Add 10 μL of

Respiration Buffer to blank control wells. Add 1–10 μL test compound to the wells. Measurement: Insert the prepared plate into a fluorescence plate reader pre-set to the measurement temperature (typically 37°C). Measure Glycolysis assay signal at 1.5 min intervals for ≥120 minutes using excitation and emission wavelengths of Ex/Em = 380/615 nm, respectively.

Safety Evaluation

Five healthy mice groups were established based on the efficacy experiment in this section: normal, positive drug (MTX, 2 mg/kg), administration of every 4 days (SWE-NMs/4, dose of 100 mg/kg for SWE), administration of every 3 days (SWE-NMs/3, dose of 100 mg/kg for SWE), administration of every 2 days (SWE-NMs/2, dose of 100 mg/kg for SWE) with intravenous administration. Normal mice were treated with an equivalent volume of saline. Two days after the last administration, the mice were euthanized and key organs including the heart, liver, spleen, lungs, and kidneys were removed for histological analysis, as previously reported. Measure the levels of alanine aminotransferase (ALT), aspartate aminotransferase (AST), creatine kinase (CK), lactic dehydrogenase (LDH), uric acid (UA), white blood cells (WBC) and red blood cell (RBC) in the serum obtained from every group mice using the Hitachi 7020 automatic biochemical analyzer (Hitachi, Japan).

Network Pharmacological Analysis

The 3D structure of "swertiamarin" was got from PubChem (https://pubchem.ncbi.nlm.nih.gov/). The files were saved in SDF format and imported into Maestro 13.5 software. The reverse molecular docking database ePharmaLib_PHASE was selected to obtain drug targets, and the target type was set for the species limit to "Homo sapiens". We collected "swertiamarin"-related targets via the Swiss Target Prediction (http://www.swisstargetprediction.ch/, ver. 2019) databases. The species were limited to Homo sapiens. Finally, the protein target names were unified, standardized and merged using the Uniport platform (http://www.uniport.org/).

Target prediction was made with "rheumatoid arthritis" as a key word through GeneCards (https://www.genecards.org/), DisGeNET (https://www.disgenet.org/home/), NCBI Gene (https://www.ncbi.nlm.nih.gov/gene/), and CTD (http://ctdbase.org/) databases. By using the VENNY2.1.0 database, we identified common targets between drugs and diseases, which were potential targets for drug therapy and rheumatoid arthritis-related diseases.

The component-target (C-T) network was built by Cytoscape (https://cytoscape.org/, ver. 3.7.2) for understanding the complex interactions between "swertiamarin" and its corresponding targets. In addition, conditions were set for the species limit to "Homo sapiens" and a high confidence score ≥0.7 to acquire the PPI network by uploading candidate targets to the STRING database (https://string-db.org/, ver. 11.0). The "swertiamarin" - "RA" intersection target information was imported into the DAVID database (https://david.ncifcrfgov/) for GO enrichment analysis (biological process (BP), molecular function (MF) and cellular components (CC)) and KEGG for pathway analysis. The three aspects of GO enrichment analysis were drawn from the top 20 entries, and the top 20 enriched pathways were used to make KEGG bubble maps.

Molecular Docking

The 3D structure of swertiamarin was downloaded from the PubChem (https://pubchem.ncbi.nlm.nih.gov/) and saved in PDB file format. We selected PyMOL 1.7.2.1 for adding hydrogen atoms to the molecular structure of swertiamarin and converted it into PDBQT files. The crystal structure of swertiamarin was taken from the PDB (http://www.rcsb.org/). Docking simulation was conducted using the AutoDock Vina software, and the lower affinity score of the swertiamarin-target was selected as the screening condition for in-depth analysis. The action patterns of swertiamarin and its corresponding goals were analyzed and visualized with Discovery Studio Visualizer.

Immunofluorescence Staining

After 2 h SWE-NMs incubation, RAW264.7 cells were washed 3 times by PBS. Then, the primary antibody of anti-EGFR (Affinity, AF6042), anti-JNK (Thermofisher, PA5-36548) and anti-MMP9 Antibody (Affinity, AF0220) dissolved in PBS with blocking buffer was added to the samples at 4°C overnight. The cells were washed by PBS and was added FITC coupled fluorescence secondary antibody at room temperature for 1 h. Cells were fixed and stained with DAPI (absin, abs47047616) for 5 min and then photographed by laser scanning confocal microscope (LSM 800, Zeiss, Germany).

Statistical Analysis

The quantitative results were provided as mean ± standard deviation. A Student's two-sided *t* test was used for statistical analysis of a two-group comparison. For multiple comparisons, a two-way analysis of variance (ANOVA) was utilized. A significant difference was considered at P value <0.05.

Results and Discussion

Characterization and Stability of SWE-NMs

FA-HA-PAE copolymer was synthesized mainly by Michael-addition polymerization and amidate reaction as previously reported.[7] The fabricated copolymer could self-assemble into nanomicelle for targeted delivery of SWE. The blank FA-HA-PAE nanomicelles (NMs) and SWE-loaded FA-HA-PAE nanomicelles (SWE-NMs) were both prepared by ultrasonic method. The content detection and methodological investigation of SWE were shown in Supplementary Material 1 – Supporting methods, Supplementary Figure 1 and 2, Supplementary Tables 1 and 2. Both the blank NMs and SWE-NMs were dispersed as spherical particles using TEM images (Figure 1D and E). The particle sizes and zeta potentials of SWE-NMs were 274.0 ± 1.5 nm and −10.15 ± 0.2 mV as measured by the Malvern Zetasizer NanoZS system, respectively (Figure 1F and Supplementary Figure 3). The PDI of blank NMs and SWE-NMs were 0.177 and 0.101, respectively. In addition, both NMs implied good in vitro stability at 4°C or 37°C in one week (Figure 1G); two types of NMs are stable in serum or plasma for at least 24 hours (Figure 1H). To evaluate the drug loading properties of polymeric nanoparticles, DL and EE were used frequently as important parameters. The DL and EE were 10.6 ± 0.7% and 68 ± 6.0%, respectively.

In vitro Integrity of NMs in RAW264.7 Cells

To monitor the integrity of polymeric micelles, DiD and DiR (the FRET pair, acting as the donor and acceptor, respectively) were encapsulated into nanomicelles (DiD/DiR-NMs). The micelles fabricated from the block copolymers with physical encapsulation of DiD and DiR were found to have a high FRET efficiency. In intact micelles, excitation energy from the DiD (donor) transferred to the DiR (acceptor) due to close proximity (<10 nm), and FRET occurs ("FRET on"), while the dissociation of micelles causes FRET to disappear ("FRET off") due to the long distance (>10 nm) between the DiD and DiR (Figure 2A). Once excited at 640 nm, the micelles containing DiD and DiR in deionized water had strong DiD fluorescence at 660 nm with equally strong DiR fluorescence at 780 nm, indicating that a strong FRET occurred. When acetone was added into the solution to dissolve the micelles, the FRET peak at 780 nm almost disappeared (Figure 2B).

The FRET effect occur on the cell membrane due to the accumulation of dialkyl carbocyanine dyes (DiD and DiR) on the membrane surface and the fluorescence resonance of the donor and recipient dyes. Dialkylcarbocyanine dyes consist of two long alkyl tails and a charged fluorophore. When the dye reaches the surface of the cell membrane, the alkyl tail inserts into the membrane lipid bilayer. The fluorescent head remains on the membrane surface and rapidly and uniformly distributes across the entire membrane surface through lateral diffusion.[26] To study the integrity of nanomicelles in vitro, LPS+IFN-γ activated RAW264.7 cells were incubated with DiD/DiR-NMs for 12 h. The data were taken by CLSM with DiD and DiR channels. The FRET signal coming from the cells was quantified by the FRET ratio to evaluate the integrity of DiD/DiR-NMs. DiD in the donor channel was excited by a 640 nm laser, and the emission was obtained at 680 nm, which was in red color fluorescence. DiR as the acceptor channel was excited at the same 640 nm for the emission of DiD, and the emission of DiR was obtained at 780 nm (FRET channel, in green color). The fluorescence was checked in different time points so that the dynamic dissociation process from polymeric micelles was monitored. As shown in Figure 2C, the intensity of DiR green light was strong and that of DiD was almost week light with the FRET ratio of 0.74, which showed that a strong FRET micelles remained intact within 30 min. With the time elongated to 6 h, the red fluorescence of DiD in the cytomembrane became stronger with the decreased FRET ratio of 0.51. After 12 h of incubation, majority cells showed red fluorescence with almost disappeared green fluorescence with FRET ratio of 0.30, indicating that most fluorescent dyes were released from the nanomicelles.

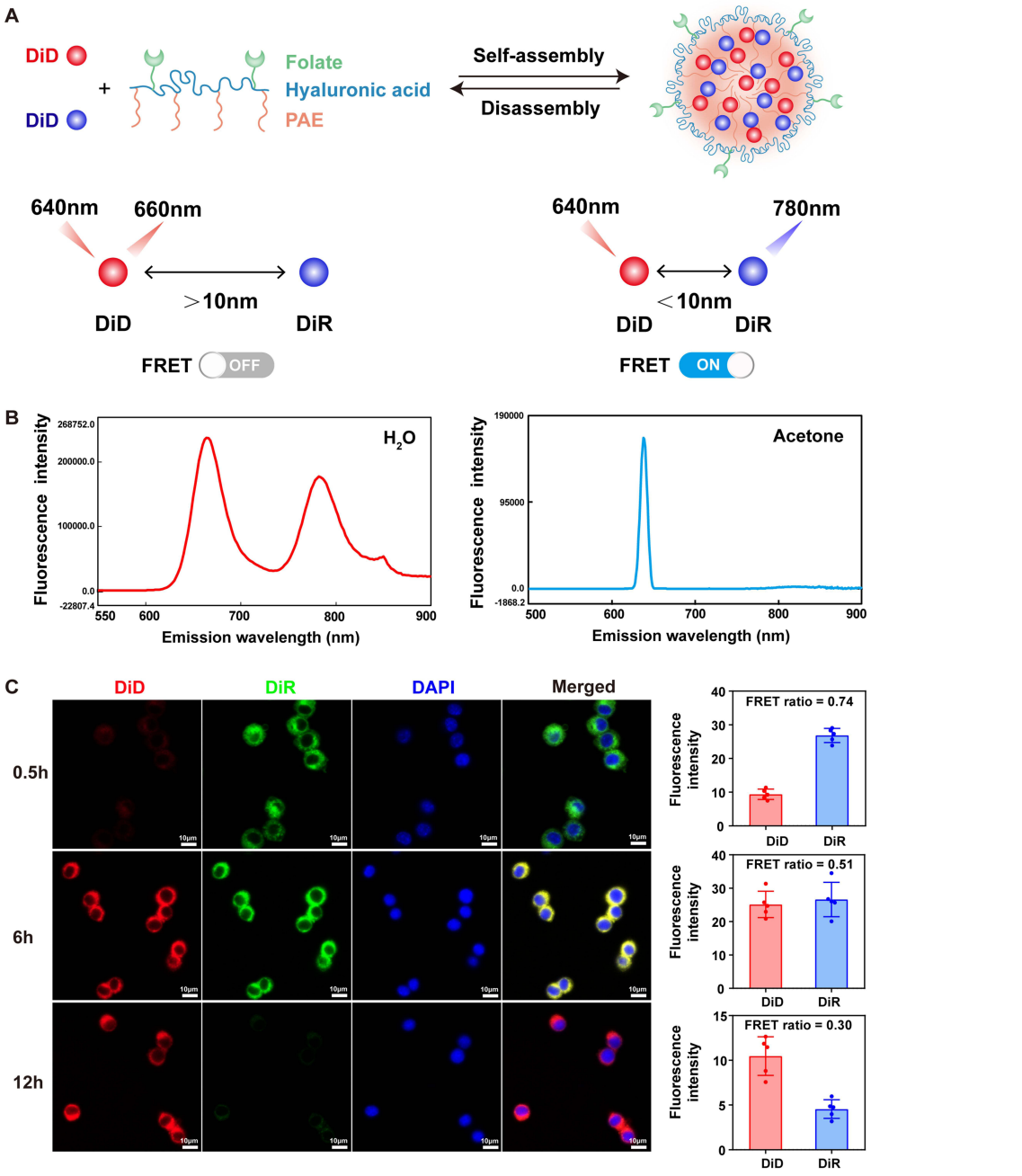

Figure 2 In vitro integrity of DiD/DiR-NMs. (**A**) Schematic diagram of the Design and working principle of DiD/DiR-NMs with FRET occurrence (FRET "on") or disappearance (FRET "off") in intact state or dissociated state. (**B**) The fluorescence spectra of the FRET nanomicelles in aqueous solution (red) or diluted with 10×acetone (blue) at 1.0 mg/mL (Ex: 640 nm/Em: 500~900 nm). (**C**) In vitro integrity of DiD/DiR-NMs in RAW264.7 cells at different time points: 0.5, 6, 12h. The red channel represented DiD channel. The green channel represented FRET channel (DiR). The FRET ratio were shown in the right columns. Scale bar = 10 μm. FRET ratio $=I_{DiR}/(I_{DiD} + I_{DiR})$, where I_{DiD} and I_{DiR} mean the fluorescence intensity of the donor (DiD) at 660 nm and acceptor (DiR) at 780 nm, respectively.

It is generally believed that proinflammatory macrophages utilize the glycolytic pathway to meet their high energy demands for proinflammatory response.[27] During this response, proinflammatory macrophages in inflamed joints switch to a hypermetabolic glycolysis state, which is called "Warburg effect" or "metabolic reprogramming". This leads to excessive lactic acid production and contribute the pH drop at the affected joint.[28] In this part, we used LPS+IFN-γ activated RAW264.7 cells to simulate this external inflammatory environment. The results shown in Figure 2C indicated that within 12 hours after the NMs reached the target tissue, 70% of the nanomicelle structures on the surface of

https://doi.org/10.2147/IJN.S511421

inflammatory macrophages was destroyed, thus releasing the loaded dyes or drugs. These results provided an in vitro research basis for precise control of the biofate of nanomicelles.

Different Pathological Characteristics of Early and Advanced-Stage Arthritis Mice

The joint destruction and synovial inflammation in AIA mice were assessed by micro-CT and histological assays. In micro-CT analysis, the ankle joints of different group mice were scanned. Compared with normal and early-stage arthritis, AIA mice at advanced-stage appeared rough bone surfaces and severe bone damage (Figure 3A). The arrow markings represented the site of bone injury. There was also a remarkable diminution in BMD and an increase in BS/BV in advanced RA mice (Figure 3B). Applying the hematoxylin and eosin (H&E) staining further showed the synovial

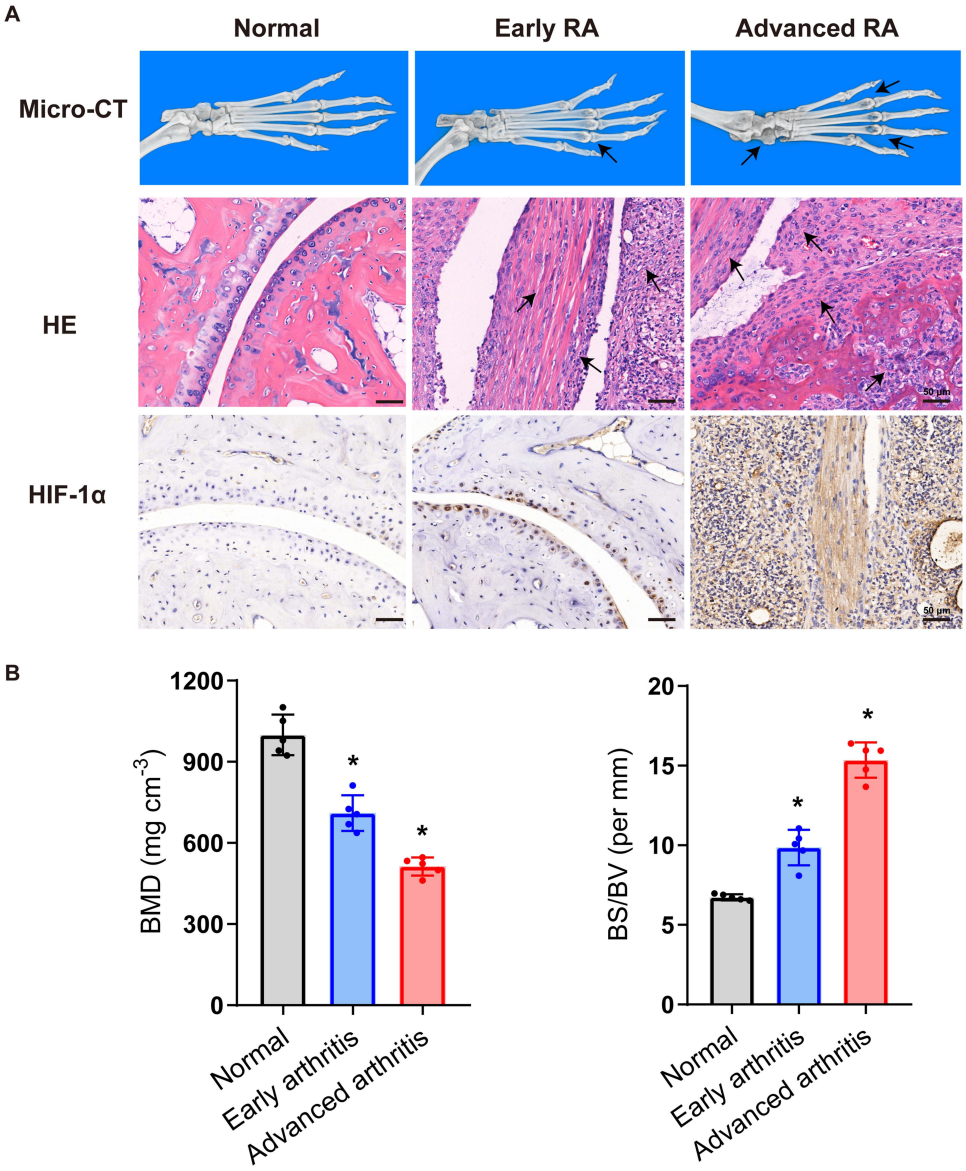

Figure 3 Different pathological characteristics of early and advanced-stage arthritis mice. (**A**) Bone erosion and synovial inflammation in early and advanced RA mice. Representative micro-CT images of ankle joints showing bone damage degree in normal mice, early-stage AIA mice, and advanced-stage AIA mice. The arrow markings represented the site of bone injury. H&E-stained showing inflammatory cell infiltration and synovial hyperplasia in the joint tissues from mice in each group (n = 5). The arrow markings represented the locations of inflammatory cell infiltration and synovial hyperplasia. Scale bar=50 μm. Immunohistochemical analyses of the hypoxia inducible factor-1α (HIF-1α) expression in the joint tissues from mice in each group (n = 5). Scale bar = 50 μm. (**B**) Quantitative micro-CT analyses of bone mineral density (BMD) and bone surface density (BS/BV) of the ankle joints at the endpoint of the experiment. *P<0.05 vs Normal group.

inflammation in the joint tissues from mice in each group (Figure 3A and Supplementary Figure 4). The arrow markings represented the locations of inflammatory cell infiltration and synovial hyperplasia. Observable, AIA mice with advanced RA represented an excessive abundance of inflammatory cell infiltration and synovial hyperplasia in the joint tissues. The rapid abnormal proliferation of immune cells and synovial cells in the joints, as well as the accompanying disordered metabolism, leading to hypoxia in the RA joint cavity.[2,29,30] Therefore, we surveyed the degree of hypoxia in the joint cavity of AIA mice by detecting the expression of hypoxia-inducible factor-1 (HIF-1α). HIF-1α is an important transcriptional regulatory factor that mediates cellular involvement in hypoxia response.[7,31] The immunohistochemical analysis indicated that mice in the early and advanced-stage arthritis group showed the up-regulated expression of hypoxia-inducible factor-1α (HIF-1α) (Figure 3A and Supplementary Figure 5). Observable, AIA mice with advanced RA assumed overexpression of HIF-1α at the ankle joints, which was consistent with the results measured by H&E staining.

Taken together, the data suggested that advanced RA exhibited more severe synovial inflammation and hypoxia. Then, are the dissociation speed and degree of the NMs the same in the RA joint cavity of the two stages? We then examined these questions in the two stages in the AIA mice model.

In vivo Integrity of NMs at Different Stage in AIA Mice Model

To investigate the integrity of nanomicelles in early and advanced-stage arthritis mice, the biodistribution of DiD/DiR-NMs was tested on AIA mice through tail vein injection. In early-stage arthritis, in vivo imaging system (IVIS) was utilized to monitor the fluorescence in major organs of mice (heart, liver, spleen, lung, kidney, and paws) at 12, 24, 48, 72, and 96 h post-injection (Figure 4A). We quantified the fluorescence intensity of AIA mice joints at different time points and calculated the FRET ratio (Figure 4B). The FRET ratio kept at 0.73 within 12 h, which meant that most of DiD/DiR-NMs were relatively stable As time extended, DiD and DiR channel displayed much stronger fluorescence intensity after administration for 24 h (the FRET ratio=0.51). At 48–72 h, DiD channel maintained strong fluorescence signal, and DiR channel fluorescence signal weakened. The data indicated that the micelle structure began to break gradually. The fluorescence of DiD channel reduced at 96 h, while the DiR fluorescence almost disappeared. The FRET ratio reached a balance at 48, 72 and 96 h with FRET ratio of 0.41, 0.33 and 0.29, respectively. In other words, the micelle structure was completely destroyed within 96 hours. To further validate the biofate of nanomicelles, DiD/DiR-NMs were intravenously injected into the rat to evaluate their integrity and circulation in blood at 5 min, 0.5, 1, 3, 6, 12, 24, 48, 72, 96 h post-injection. As shown in Figure 4C, the DiD/DiR-NMs kept at a high FRET ratio of 0.89. At 3 h, the FRET ratio of DiD/DiR-NMs decreased to 0.67. Until 72 h, the FRET ratio remained around 0.33 (0.59, 0.52, 0.48, 0.40 at 6, 12, 24, 48 h, respectively). At 96 h, the FRET ratio reduced to 0.25, illustrating that 75% DiD/DiR-NMs micelles had been disassembled in the blood.

Differently, the detection time points were 6, 12, 24, 48, and 72 h after injection in advanced-stage arthritis mice. From Figure 4D, compared with the saline group, mice injected with DiD/DiR-NMs showed significantly higher levels of inflammatory joint accumulation 6 h. After 12 h of administration, DiD and DiR channels showed stronger fluorescence intensity, indicating their targeting and long-term accumulation at inflamed joints. During 48 h, DiD channel maintained strong fluorescence signal, while DiR channel had weak fluorescence signal. The fluorescence of DiD channel reduced at 72 h with almost disappeared DiR fluorescence. The FRET ratio decreased from 0.53 to 0.13 within 72 h, indicating that nanomicelles gradually break down in the inflammatory micro-environment, leading to the release of the dye (Figure 4E). DiD/DiR-NMs were intravenously injected into rats to evaluate their integrity in blood at different time points (5 min, 0.5, 1, 2, 4, 6, 12, 24, 48, 72 h post-injection). As shown in Figure 4F, the DiD/DiR-NMs kept at a high FRET ratio of 0.76. The FRET ratio decreased to 0.51 and remained around 0.49 within 48 h (0.52, 0.49, 0.45, 0.49 at 6, 12, 24, 48 h, respectively). At 72 h, the FRET ratio reduced to 0.37, illustrating that most DiD/DiR-NMs micelles had been disassembled in the blood of rats.

The above results indicated that compared to early-stage arthritis, nanomicelles remained intact and released dyes for a shorter time in advanced-stage arthritis of AIA mice model. Generally, the inflamed joint cavities had a lower pH and the pH values varied at different stages of RA.[32] In the microenvironment of RA joints, a large number of immune cells

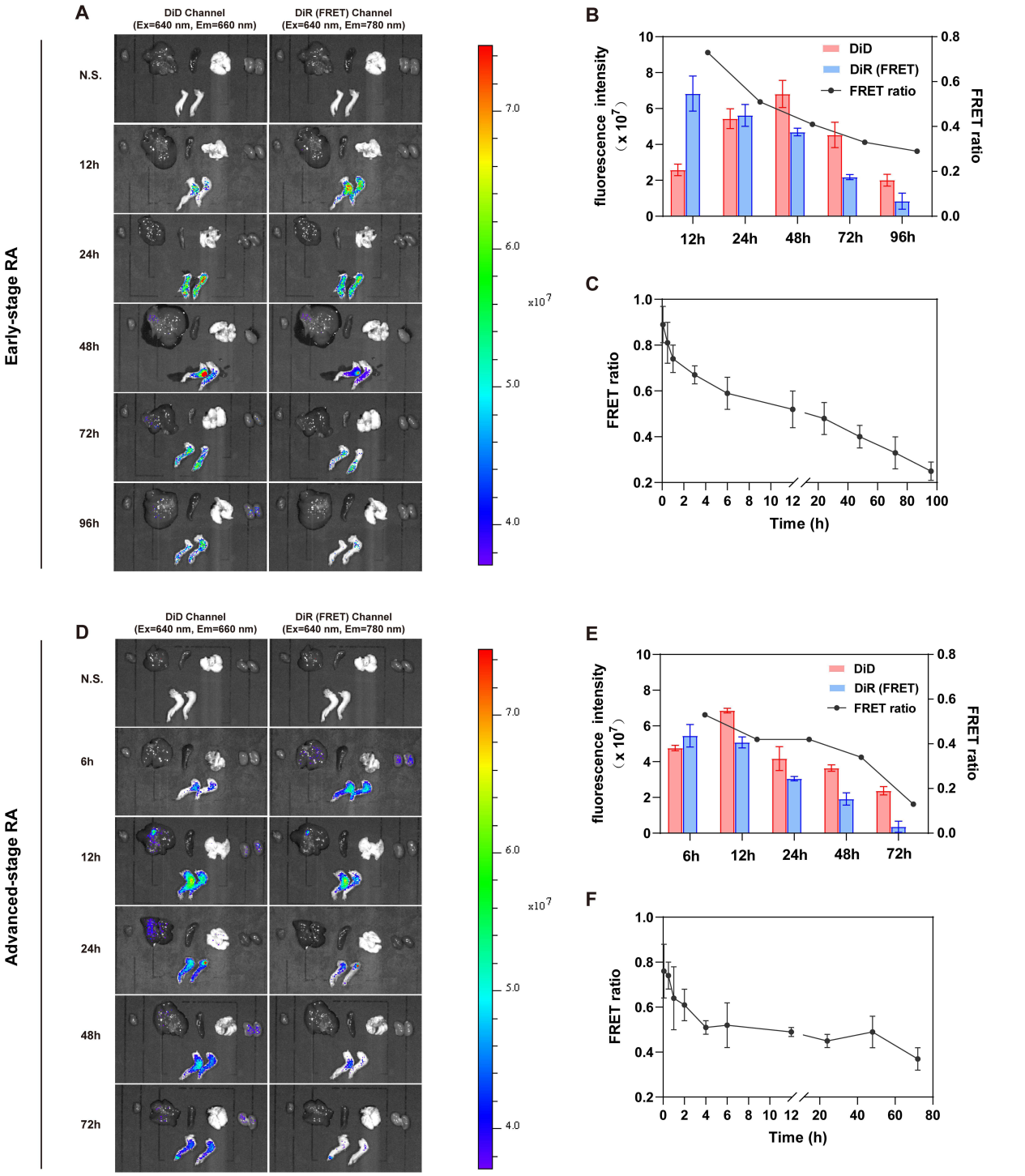

Figure 4 In vivo integrity of DiD/DiR-NMs at early-stage arthritis (**A**–**C**) and advanced-stage arthritis (**D**–**F**) in AIA mice model. (**A**) Mice were i.v. injected with DiD/DiR-NMs and imaged at 12, 24, 48, 72, and 96 h and then sacrificed and dissected. (**B**) The statistical graphs of the fluorescence intensity in the paw of mice based on the semi-quantitative analysis and average FRET ratios at different time. (**C**) DiD/DiR-NMs were intravenously injected into mice to evaluate their integrity in blood at different time points (5 min, 0.5, 1, 3, 6, 12, 24, 48, 72, 96 h post-injection). After injection, mice plasma samples were detected by fluorescence spectrophotometer to calculate the FRET ratio. (**D**) Mice were i.v. injected with DiD/DiR-NMs and imaged at 6, 12, 24, 48, and 72 h and then sacrificed and dissected. (**E**) The statistical graphs of the fluorescence intensity in the paw of mice based on the semi-quantitative analysis and average FRET ratios at different time. (**F**) DiD/DiR-NMs were intravenously injected into mice to evaluate their integrity in blood at different time points (5 min, 0.5, 1, 2, 4, 6, 12, 24, 48, 72h post-injection). After injection, mice plasma samples were detected by fluorescence spectrophotometer to calculate the FRET ratio. Ex vivo live imaging of DiR distribution in heart, liver, spleen, lung, kidney, and joints in AIA mice by detecting DiR fluorescence intensity with IVIS system. The parameter settings of the imaging were Ex: 640 nm, Em: 660 nm for the DiD (donor) and Em: 780 nm for DiR (acceptor). The DiD channel represents the disassociated DiD, and the FRET (DiR) channel represents the intact FRET NMs. FRET ratio = $I_{DiR}/(I_{DiD} + I_{DiR})$, where I_{DiD} and I_{DiR} mean the fluorescence intensity of the donor (DiD) at 660 nm and acceptor (DiR) at 780 nm, respectively.

such as macrophages and T cells underwent metabolic reprogramming and rapid synovial proliferation, when oxygen consumption and hypoxia rapidly increased.[33] Cells therefore used the glycolytic pathway to meet the high energy requirements of their pro-inflammatory response. This leaded to excessive production of lactic acid, a product of glycolysis, and caused the pH of the affected joints to drop.[7] In this study, the hydrophobic group of nanomicelle was pH sensitive material PAE,[34] which leaded to its different release degree in early and advanced-stage arthritis mice. Therefore, the pathologic characteristics of different stages of arthritis should be fully considered when the nanomicelles were used for RA treatment.

In vivo Integrity of NMs in Zebrafish Larval Inflammatory Model

Zebrafish shows tremendous advantages as a valuable preclinical model, which allows rapid screening and in situ tracing of polymeric micelles.[35] To get stronger visualization, zebrafish at 3 dpf were used in this study. Intact DiD/DiR-NMs entered into zebrafish after 30 min incubation, where DiR emission (green fluorescence) was clearly observed (Supplementary Figure 6A). As shown in Supplementary Figure 6B and C, a strong FRET signal with a FRET ratio of 0.77 was observed at 30 min, which indicated that the majority of the nanoparticles remained intact. Over time, the green fluorescence significantly decreased, presumably due to the breakdown of the DiD/DiR-NM, followed by a significant increase in red fluorescence (caused by a release of DiD) at 6 h. The FRET ratio decreased from 0.53 to 0.48 from 8 to 24 h. Importantly, a very low FRET signal still existed at 48 h postincubation with a FRET ratio of 0.35, suggesting that there was still a small amount of DiD/DiR-NMs remaining intact in vivo. In this study, the data of zebrafish larval inflammatory model revealed that about half of the NMs remained intact within 24h after administration, a result consistent with integrity in AIA mice model. The difference was that about 40% of the NMs were still intact in mice at 48 h after administration, while most of the micelles in zebrafish were destroyed and the dye was released.

The Therapeutic Efficacy of Different Administration Intervals of SWE-NMs in AIA Mice With Advanced RA

Due to the fact that RA was generally a chronic disease,[36] we focused on the therapeutic efficacy of SWE-NMs on AIA mice with advanced RA. Consistent with the in vivo integrity assessment, we set up two different dosing interval groups (every 72 h and every 96 h) in this section.

The schematic illustration of SWE-NMs treatment was shown in Figure 5A. In Figure 5B and C, the AIA model group displayed severe swelling in the joints, whereas the SWE-NMs/3 treated group presents a better change in joint diameter, suggesting a successful inhibitory effect in paw thickness of swollen joints. SWE-NMs/3 and MTX reduced arthritis index compared with the normal group (Figure 5D). By pathological detection, as assessed by H&E staining, synovial inflammation was significantly reduced in the SWE-NMs/3 and MTX injection groups (Figure 5E). The safranin O/fast green and toluidine blue staining could evaluate the extent of articular cartilage damage by labeling the glycosaminoglycans in tissues.[37,38] From Figure 5F and G and Supplementary Figure 7 and 8, the AIA group mice manifested severe cartilage destruction in the ankle joint stained. In contrast, the cartilage boundaries of the mice treated with SWE-NMs/3 and MTX were clearer than those of the AIA group, which was comparable to the healthy group.

We already confirmed that hypoxia varies at different stages of arthritis (Figure 3), so it was necessary to measure the metabolic levels of cells. Immune cells, such as pro-inflammatory macrophages, often rely on the glycolytic pathway to produce energy rather than through oxidative phosphorylation.[39] RA joint cavities appear acidic due to the fact that they produce large amounts of lactic acid through the process of glycolysis, which is released extracellular, resulting in acidification of the local environment.[28,40] Therefore, by detecting extracellular acidification rate (ECAR) and lactate level in joint tissue of every group, the glycolytic activity could be indirectly reflected. As shown, ECAR in AIA group was 2.6-fold higher than the normal group (Figure 5H). After MTX and two dose of SWE-NMs treatment, the ECAR significantly decreased. Similarly, SWE-NMs also reduced lactate production in a dose-dependent manner, which was an important product during glycolysis (Figure 5I). As an important indicator reflecting the progression of arthritis, inflammatory cytokines were also detected. From Figure 5J–L, SWE-NMs/3 and MTX prominently down-regulated

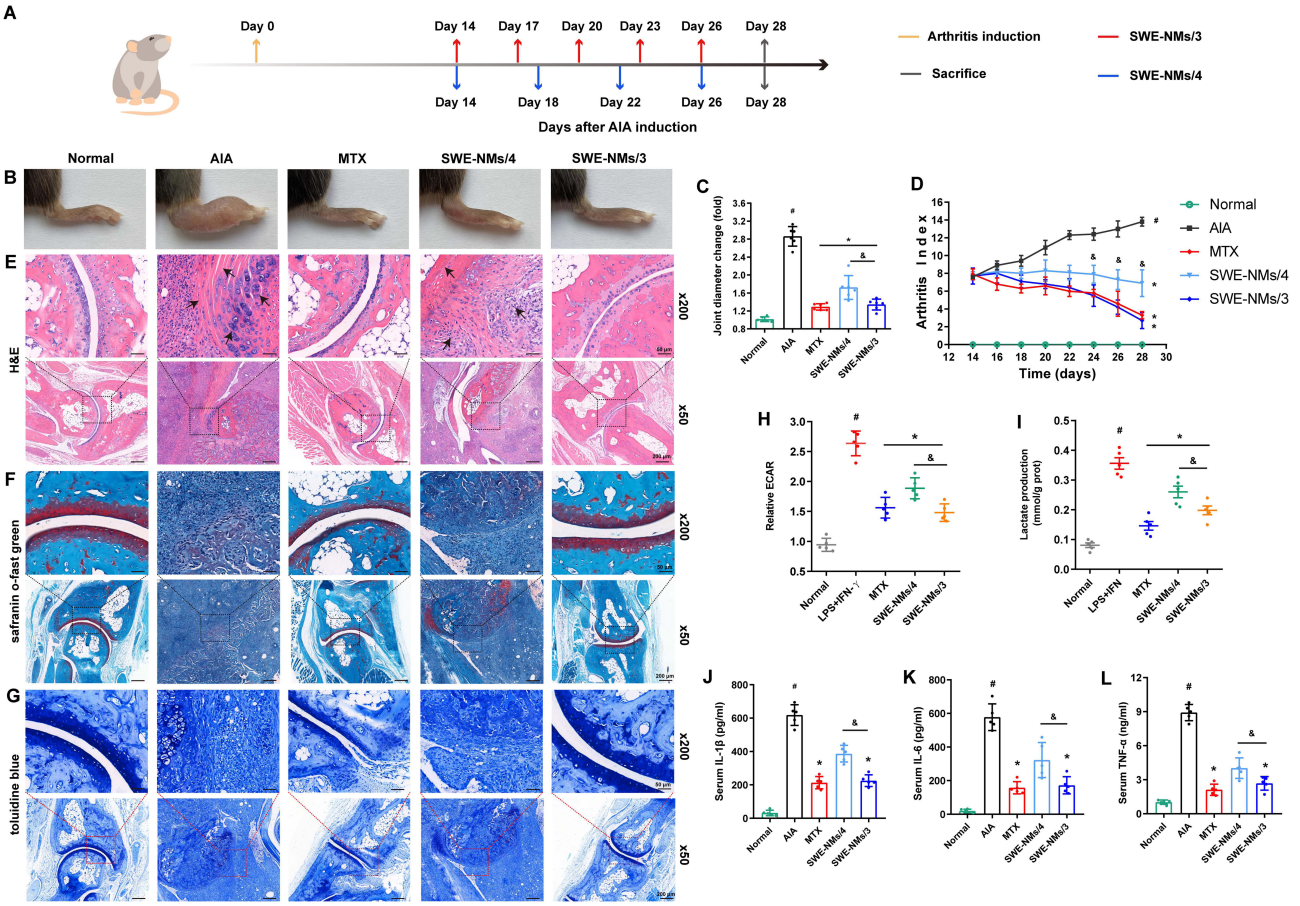

Figure 5 The therapeutic efficacy of different administration intervals of SWE-NMs in AIA mice with advanced RA. (**A**) The schematic illustration of SWE-NMs treatment. (**B**) Representative photographs of hindlimbs at the endpoint of the experiment from different treatment groups. (**C**) The paw thickness of AIA mice were recorded every other day during the treatment period. (**D**) Arthritis index of every groups were recorded every other day during the treatment period. (**E**) Histopathology evaluation of ankle joints was identified using H&E. The arrow markings represented the locations of inflammatory cell infiltration and synovial hyperplasia. Scale bar=50 μm. Detection of cartilage injury of rats ankle joint in each group by safranin o-fast green staining (**F**) and toluidine blue staining (**G**). Scale bar = 50 μm. (**H** and **I**) The histogram of ECAR and lactate levels in different groups. The production of ECAR and lactate could reflect the glycolysis ability. (**J**–**L**) Serum levels of IL-1β, IL-6 and TNF-α in every group mice were analyzed by the ELISA kits. Data represent mean ± SD (n = 5 independent animals). $^{\#}$ P<0.05 vs Normal group; * P<0.05 vs AIA group; $^{\&}$ P<0.05 SWE-NMs/4 vs SWE-NMs/3.

the expression serum levels of IL-1β, IL-6 and TNF-α, suggesting that SWE-NMs/3 possessed striking ability to reduce inflammatory response. These results indicated that SWE-NMs/3 had a potent effect on RA treatment.

The progression and development of AIA were blocked in an administration frequency-dependent manner. In the measurement of paw thickness, arthritis index and inflammatory cytokine levels, SWE-NMs/4 slightly reduced the severity of arthritis in AIA mice. The pathological examination also confirmed that SWE-NMs/4 weakly improved synovial inflammation and cartilage injury of AIA mice. Hence, the administration intervals based on the integrity assessment of NMs was reasonable. Here, we obtained the accumulation time of NMs in inflammatory joints by examining their integrity and applied these findings to improve treatment outcomes by setting reasonable dosing frequencies. As a result, we achieved good anti-RA effects. Our findings contribute to elucidate the in vivo fate of nanomedicines and provide guidance for effective drug delivery. So, is it better to have a shorter interval of administration?

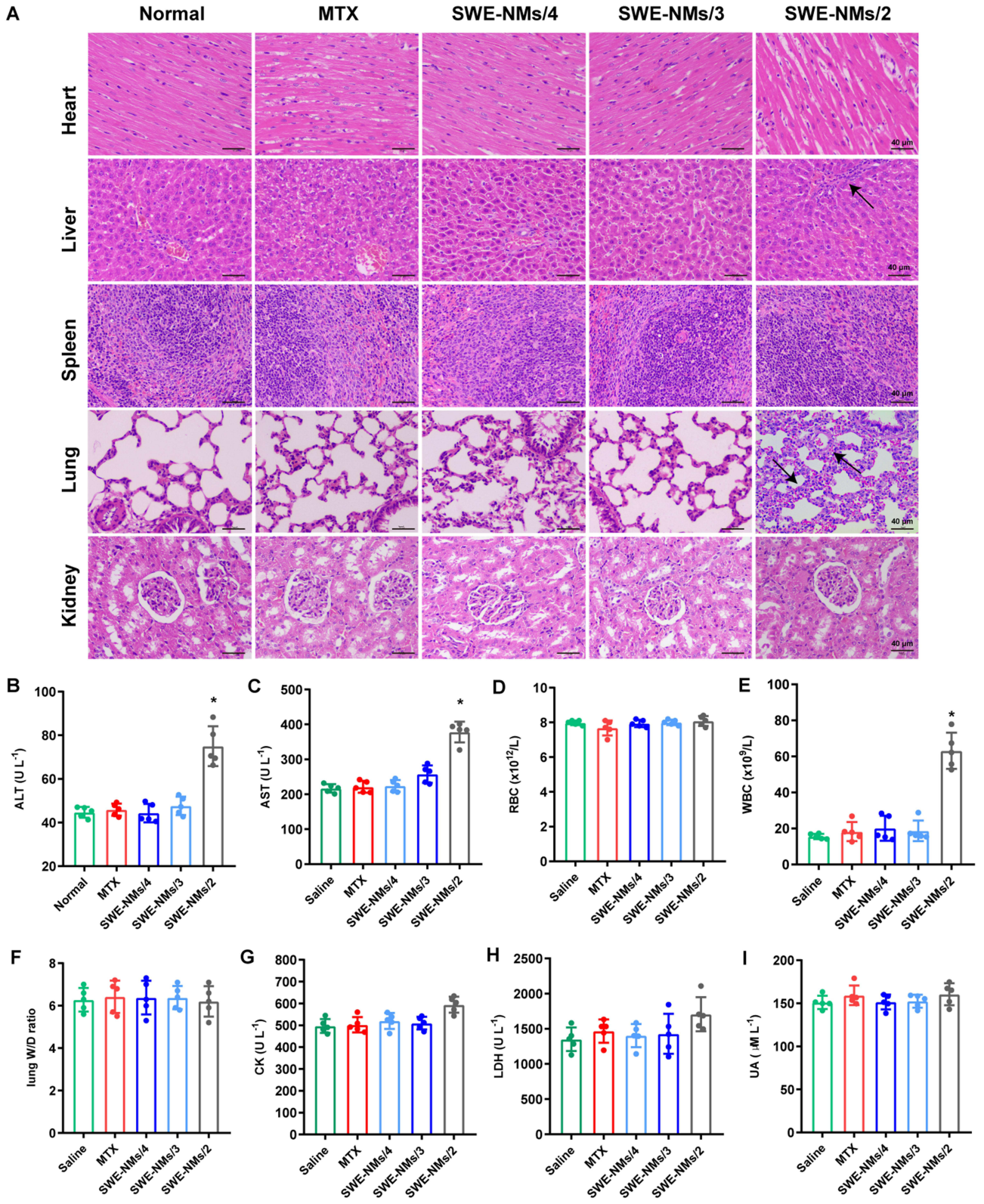

Figure 6 Preliminary safety evaluation of SWE-NMs. HE staining of the major organs (heart, liver, spleen, lung, kidney) after mice receiving the indicated treatment (**A**). The arrow markings represented the locations of hepatocellular nucleus shrinkage, liver inflammation and injury. (Scale bar = 40 μm) (n = 5 independent animals). The serum level of ALT (**B**), AST (**C**), RBC (**D**), WBC (**E**), lung W/D weight ratio (**F**), CK (**G**), LDH (**H**), UA (**I**), in mice receiving the indicated treatment. Data represent mean ± SD (n = 5 independent animals). * P<0.05 vs Normal group.

Abbreviations: ALT, alanine aminotransferase; AST, aspartate aminotransferase; CK, creatine kinase; LDH, lactic dehydrogenase; lung W/D weight ratio, lung wet weight/dry weight ratio, UA, uric acid; RBC, red blood cell; WBC, white blood cell.

https://doi.org/10.2147/IJN.S511421

Preliminary Safety Evaluation of SWE-NMs

Therapeutic scope should be defined in terms of monitoring effectiveness and avoiding toxicity.[41] In this part, we focused on whether different dosing intervals affected the main organs of mice. H&E staining was used to evaluate the histopathology of major organs. SWE-NMs/2 group caused hepatocellular nucleus shrinkage, liver inflammation and injury, which might be attributed to the toxicity of drug accumulation caused by short dosing intervals (Figure 6A). To re-examine whether SWE-NMs/2 group had adverse effects on the liver, we tested two important indicators of liver function, alanine aminotransferase (ALT) and aspartate aminotransferase (AST). The results expressed that the SWE-NMs/2 group observably up-regulated the levels of ALT and AST, while others did not change the levels of both indicators (Figure 6B and C). In Figure 6D and E, the levels of white blood cells (WBC) raised notably in the SWE-NMs /2 group, which might be a manifestation of an acute reaction caused by liver damage. Thus, as the liver was the main metabolic organ of drugs,[42] short dosing intervals could easily lead to liver toxicity. Additionally, the SWE-NMs/2 group appeared to have a slight impact on the lungs of mice (Figure 6A and F). Previously, it was reported that drug-induced pulmonary toxicity manifested as acute reactions, such as acute ARDS like reactions in drug overdose and more subtle reactions during routine treatment.[43] Moreover, we detected the cardiac function indexes creatine kinase (CK) and lactic dehydrogenase (LDH), as well as the renal function indicator uric acid (UA) levels in each group. The data demonstrated no significant changes in the hearts and kidneys of each group (Figure 6G–I). Conversely, SWE-NMs/3 and SWE-NMs/4 groups displayed no markedly congestion, necrosis, or inflammation in major organs.

Overall, the results above confirmed that shorter dosing intervals might lead to liver toxicity and lung injury. In other words, it was effective and safe to administer the drug every three days according to the integrity of nanomicelles at different times in inflammatory joints. Of course, the more accurate administration interval still needs to be determined in combination with the pharmacokinetic parameters of SWE. We will explore this issue in the next study.

Network Pharmacological Analysis

In order to further elucidate the therapeutic mechanism of SWE on RA, we conducted network pharmacology and molecular docking analysis. A total of 27 potential targets of SWE were acquired through ePharmaLib_PHASE database, and 56 related targets were obtained according to Swiss Target Prediction platform. The protein target names were then unified and standardized on the Uniport platform (http://www.uniport.org/). The results of the two databases were merged and duplicate targets were removed, resulting in 80 related targets. RA-related targets from GeneCards, DisGeNET, NCBI Gene and CTD databases were intersected, and finally 1130 RA-related targets were identified. The intersection of SWE and RA target genes resulted in a total of 20 targets. The Venn diagram of the intersecting target genes was shown in Figure 7A. These targets were primarily related to signal transduction (EGFR, ITGB1, LGALS3, MCL1, CDK2, HSPA8, ADORA2A, ADORA3), immune responses (HSPA5, MAPK1, ADA, LGALS9), matrix degradation (MMP9, MMP1, MMP3), metabolic process (HK2), and diabetes-related diseases (DPP4, GSK3β, ADAM17).

We then used STRING database to construct Protein–Protein Interaction (PPI) networks to analyze the functional relationships of relative proteins (Figure 7B). The PPI network revealed that the most concentrated proteins were involved in signal transduction, cell–cell interactions, and matrix metalloproteinases, among others (Table 1). In Figure 7C, the results of GO enrichment suggested that the biological processes (BP) were mainly concentrated in: intercellular interactions and collagen degradation. The cell composition (CC) mainly concentrated in: extracellular matrix, cell junction and secretions. The molecular functions (MF) mainly focus on metalloproteinases, proteases, kinases and so on. A total of 39 signal pathways were obtained by KEGG pathway analysis, mainly involving lipid and atherosclerosis pathways, IL-17 signaling pathway and other pathways. The top 20 KEGG pathways associated with RA were selected for bubble mapping (Figure 7D). The drug-target-pathway network was shown in Figure 7E. Overall, we determined the key target proteins according to the network topology values. Ranked by the Degree, the top 3 were selected as key targets for the swertiamarin treatment of RA, namely EGFR, MMP9, and ITGB1.

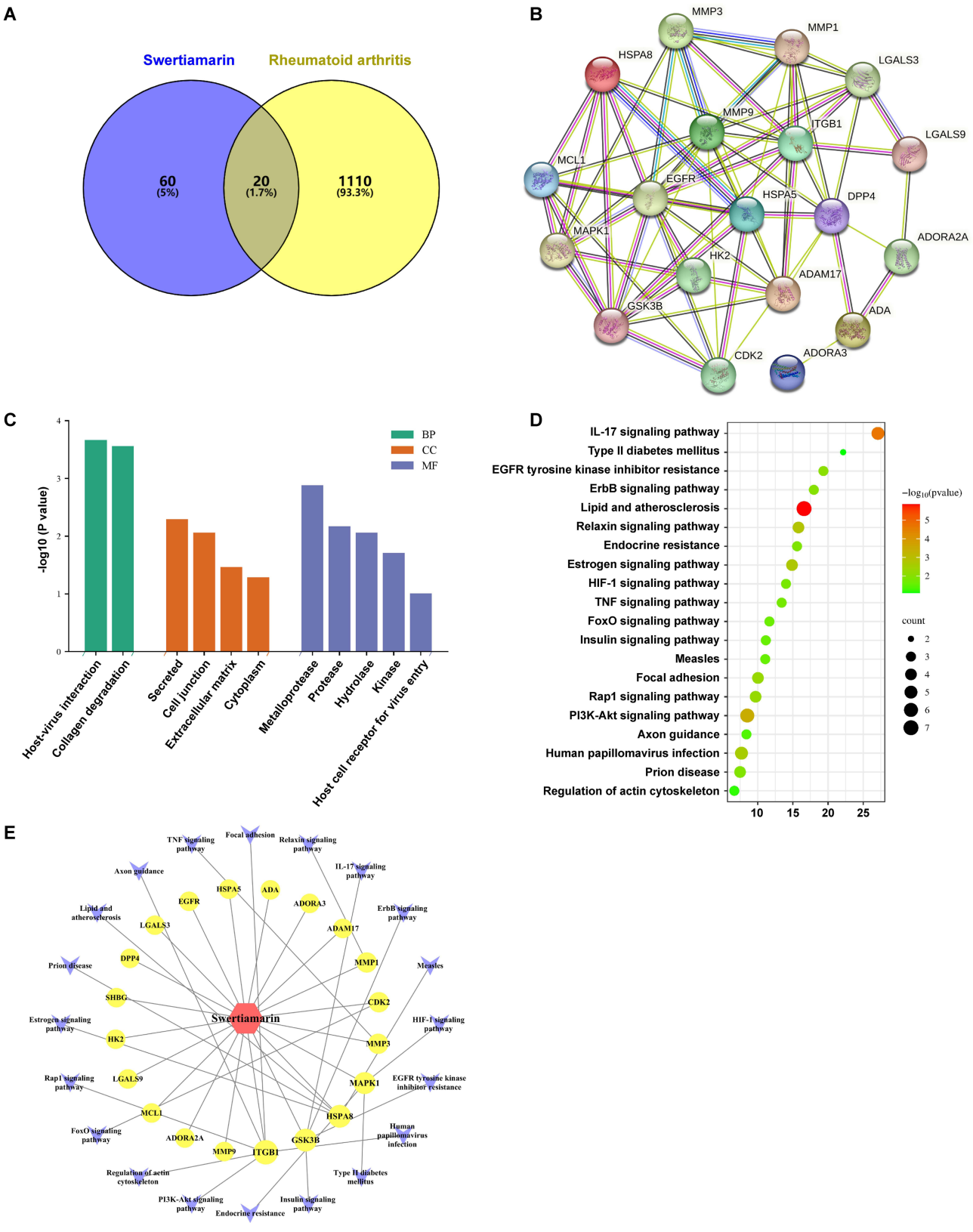

Figure 7 Network pharmacological analysis. (**A**) Venn diagram of the intersection between swertiamarin targets and RA. (**B**) The PPI network of key targets, the different colored nodes represent different proteins. (**C**) GO functional enrichment analysis. (**D**) KEGG pathway enrichment analysis. (**E**) The drug-target-pathway network of swertiamarin treatment for RA.

https://doi.org/10.2147/IJN.S511421

Table 1 Detailed Information on Twenty Proteins Arranged According to Degree

Key Targets	Degree	Betweenness Centrality	Closeness Centrality
EGFR	26	0.13	0.67
MMP9	24	0.087	0.72
ITGB1	20	0.11	0.67
GSK3B	20	0.060	0.60
DPP4	18	0.28	0.64
HSPA5	16	0.043	0.60
ADAM17	16	0.037	0.62
MMP1	16	0.019	0.62
LGALS3	14	0.039	0.60
MAPK1	14	0.010	0.53
MMP3	14	0.0074	0.55
MCL1	14	0.0057	0.53
CDK2	12	0.021	0.56
HSPA8	12	0.0075	0.53
ADA	6	0.11	0.44
ADORA2A	6	0.017	0.44
LGALS9	6	0.014	0.46
HK2	4	0	0.42
ADORA3	2	0	0.31

Molecular Docking Analysis

In order to test the reliability of the predicted interaction between swertiamarin and top 3 key targets (EGFR, MMP9, and ITGB1), AutoDock Vina 1.1.2 was used for molecular docking. In view of the signal transduction role of MAPK in the pathogenesis of RA,[25] we also conducted molecular docking between three proteins of the MAPK family (ERK, p38, JNK) and swertiamarin in this study. The affinity of receptor-ligand binding could be determined by the binding energy level in the molecular docking results. If the binding energy was less than −5.0 kcal/mol, it represented a good binding activity between swertiamarin and targets. The lower the binding energy, the better the docking effects.[44]

As shown in Figure 8 and Table 2, the data manifested that EGFR, JNK and MMP9 exhibited higher degrees of binding activity, with values of −7.1, −7.9 and −7.5 kcal/mol, respectively. The results suggested that EGFR, JNK and MMP might be the targets of swertiamarin in RA treatment while also confirming the reliability of the interaction predicted via network pharmacological analysis. However, there were limitations to predicting the core targets of SWE-NMs by network pharmacology and molecular docking. For example, it could neither reflect the actual binding strength of drug to the target proteins nor clarify the correlation between its concentration and efficacy. Therefore, the targets of these predictions needed to be further explored and verified.

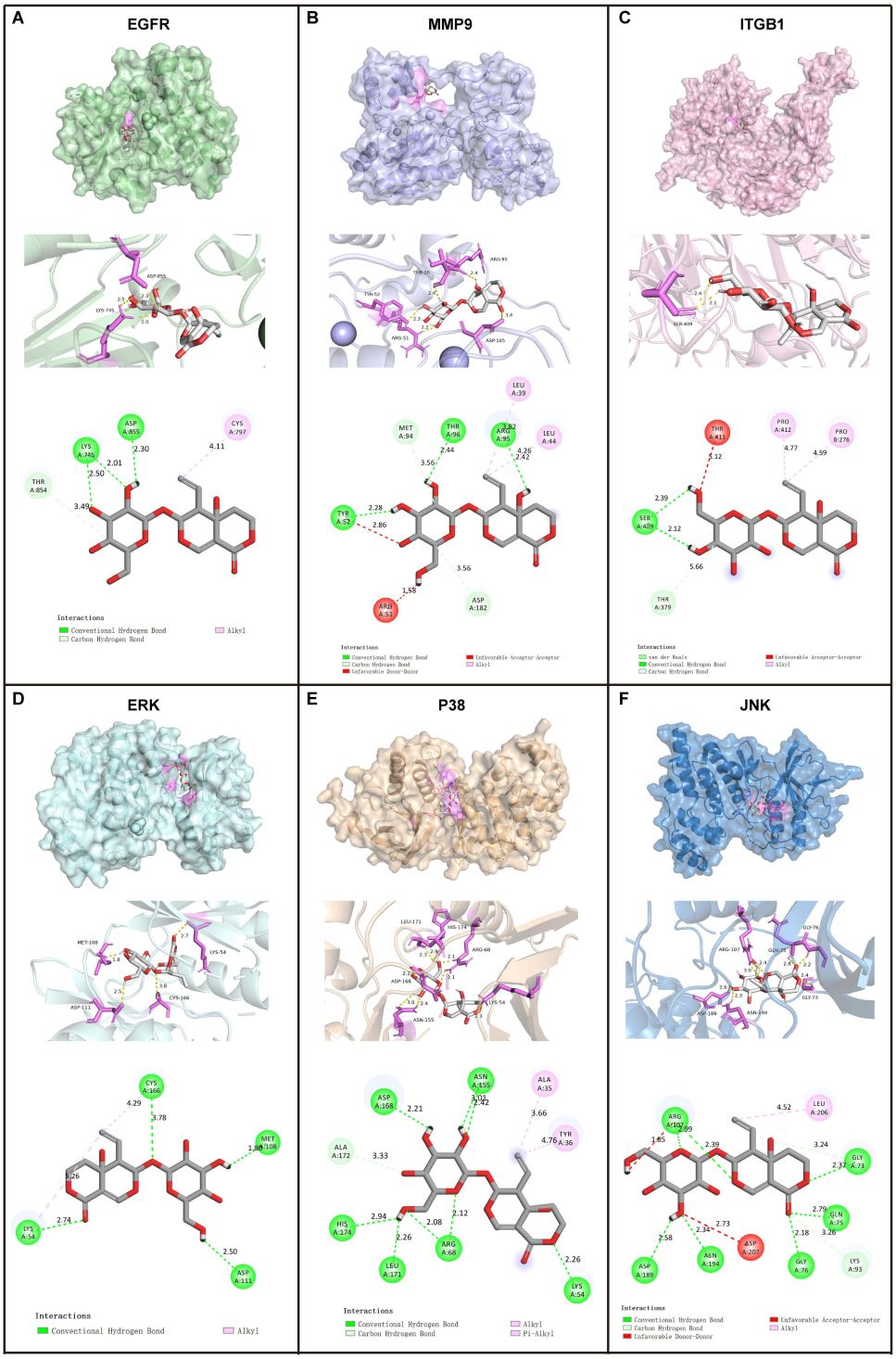

Figure 8 Molecular docking analysis. Schematic diagrams (3D and 2D) of the binding modes of representative swertiamarin-targets: EGFR (**A**), MMP9 (**B**), ITGB1 (**C**), ERK (**D**), p38 (**E**), JNK (**F**).

The Effects of SWE-NMs on Expression of EGFR, JNK and MMP9

We validated the effects of SWE-NMs on EGFR, JNK and MMP9 expression in vitro. Firstly, the cytotoxicity of free SWE and SWE-NMs was evaluated using RAW264.7 cells (Supplementary Figure 9). The results declared that the cell survival rate descend from 80% at 80 μM to 50% at 100 μM in a dose-dependent manner. Thus, SWE had a certain

https://doi.org/10.2147/IJN.S511421

Table 2 Docking Scores Between Swertiamarin and Six Core Targets

Protein	PDB ID	Affinity (kcal/mol)	Hydrogen Bond
EGFR	1XKK	−7.1	ASP855(2.3 Å), LYS745(2.0 Å , 2.5 Å)
MMP9	1L6J	−7.5	ARG95(2.4 Å), THR96(2.4 Å), TYR52(2.3 Å)
ITGB1	4WK0	−7.1	SER409(2.1 Å , 2.4 Å)
ERK	1PME	−7.5	ASP111(2.5 Å), CYS166(3.8 Å), LYS54(2.7 Å), MET108(1.8 Å)
P38	3COI	−7.1	ARG68(2.1 Å , 2.1 Å), ASN155(2.4 Å , 3.0 Å), ASP168(2.2 Å), HIS174(3.0 Å), LEU171(2.3 Å), LYS54(2.3 Å)
JNK	4Y46	−7.9	ARG107(2.4 Å , 3.0 Å), ASN194(2.3 Å), ASP189(2.6 Å), GLN75(2.8 Å), GLY73(2.4 Å), GLY76(2.2 Å)

degree of cytotoxicity, and two doses of 30 μM and 60 μM were selected in the appropriate concentration range for subsequent evaluation in this study.

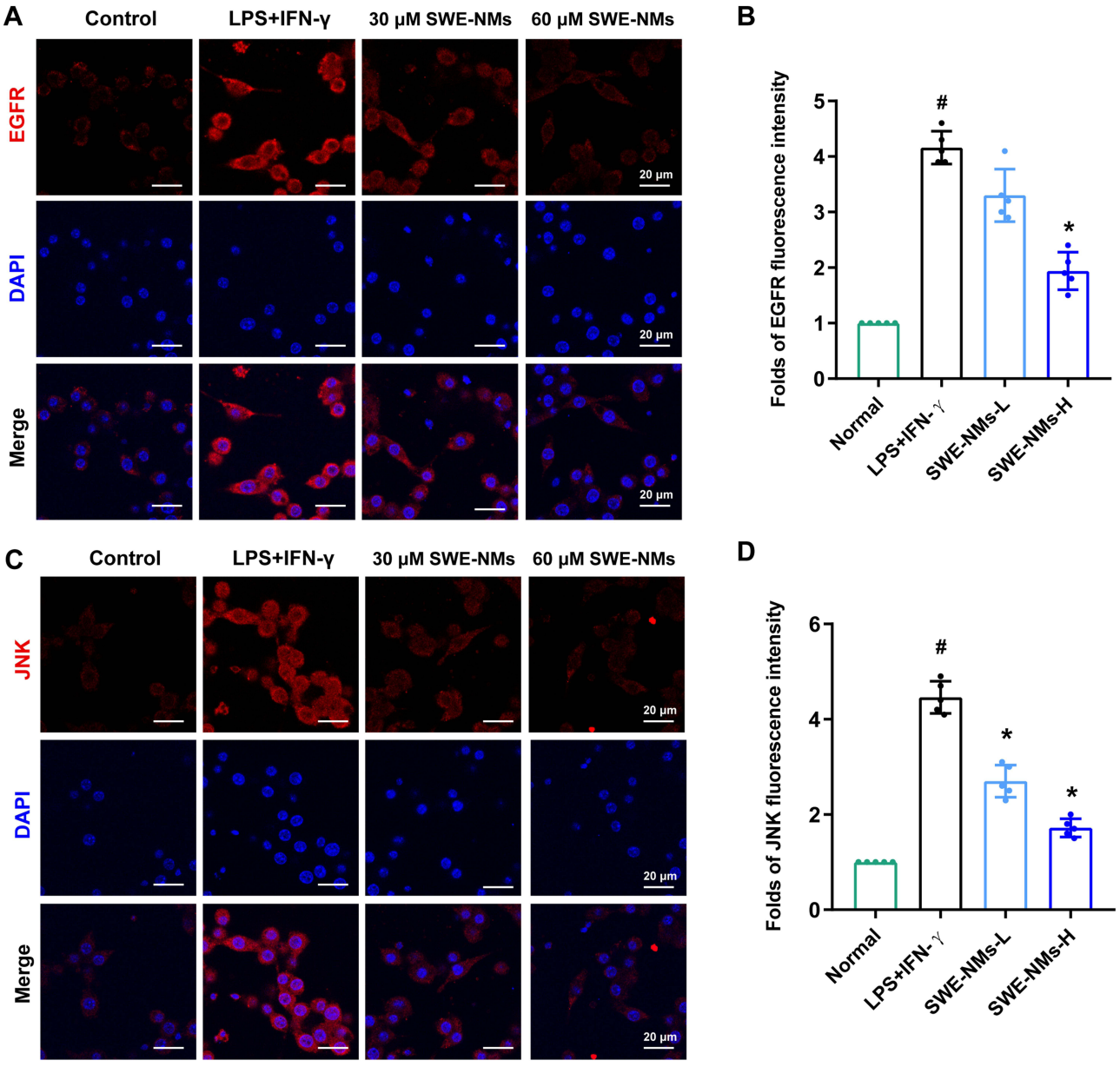

Figure 9 Continued.

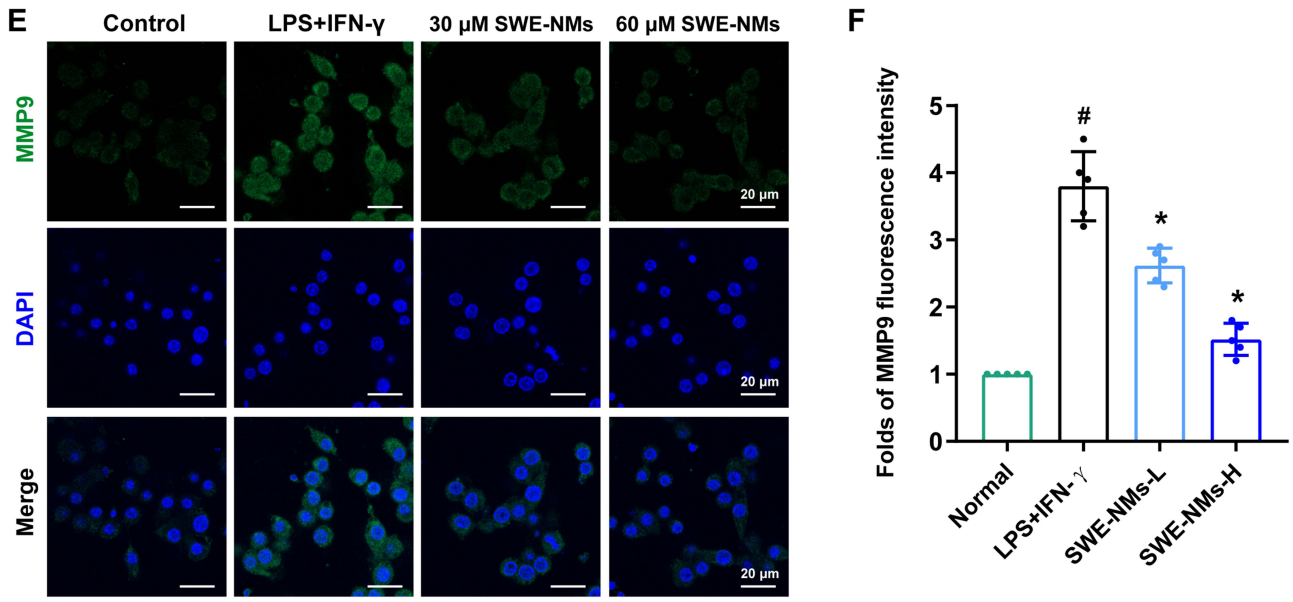

Figure 9 The effects of SWE-NMs on expression of EGFR (**A** and **B**), JNK (**C** and **D**) and MMP9 (**E** and **F**). Immunofluorescence staining of EGFR (red), JNK (red), MMP9 (green) and nuclei (blue) on RAW264.7 cells in different groups. Scale bar=20 μm. The statistical graphs of the expression of EGFR, JNK and MMP9 based on semi-quantitative analysis of the in vitro fluorescence images after i.v. administration of SWE-NMs in RAW264.7 cells. Statistical significance was determined by two-sided Student's *t*-test. Data represent mean ± SD. # $P < 0.05$ vs Normal group; * $P<0.05$ vs LPS+IFN-γ group.

In Figure 9A–F, immunofluorescence experiments showed that compared with control group, the expression of EGFR (Figure 9A and B), JNK (Figure 9C and D), and MMP9 (Figure 9E and F) strikingly elevated in LPS+IFN-γ-induced RAW264.7 cells. Treatment with 30 μM SWE-NMs markedly inhibited the levels of three proteins, while 60 μM SWE-NMs had a stronger effect. The results indicated that SWE-NMs repressed on the expression of EGFR, JNK and MMP9 in a concentration dependent manner. As a therapeutic target for RA, synovial hyperplasia overexpressed EGFR and its ligands.[21] EGFR blocker lapatinib inhibited the synthesis of matrix metalloproteinases from synovial fibroblasts.[45] In downstream targets of the EGFR pathway, JNK was a vital target for the treatment of RA by inhibiting MMP3.[46] Zhao also confirmed that angiotensin II upregulated RANKL/NFATC1 expression in synovial cells from patients with RA through the ERK1/2 and JNK pathways.[47] Thus, we revealed that SWE-NMs might improve RA symptoms by blocking the EGFR/JNK/MMP9 pathway.

Conclusion

In summary, the self-assembly of poorly water-soluble drugs and polymer nanomicelles is a dynamic process that can lead to unwanted drug release when exposed to serum. This is due to drug exchange with plasma proteins including albumin and high-density lipoprotein, which reduces the drug delivery efficiency of nanomicelles. In this work, we aimed to understand the biofate of RA-targeting nanomicelles loaded with SWE for better administration planning and to investigate the therapeutic mechanism of SWE. Through in vitro and in vivo FRET imaging, on cellular level, the nanomicelles could enter inflammatory cells and completely release most cargoes in 12 h, while in animals, the majority of nanomicelles was destroyed within 72 h. Hence, we tailored the administration scheme of SWE-NMs for RA treatment. As expected, injection every 3 days (SWE-NMs/3) displayed enhanced accumulation in arthritic joints and strong anti-RA therapeutic effect, as well as good safety profile. Of course, the more accurate administration interval still needs to be determined in combination with the physicochemical parameters of SWE. We will explore this issue in the next study. In addition, network pharmacology and molecular docking analysis revealed that SWE-NMs might work by blocking the EGFR/JNK/MMP9 pathway. These resulted in increased delivery efficiency and improved anti-RA efficacy. Therefore, our findings are not only important for understanding the in vivo fate of nanomicelles but also for guiding the improvement of nanoparticle drug delivery strategies.

https://doi.org/10.2147/IJN.S511421

Funding

This work was supported by the Joint Fund for Regional Innovation Development of the National Natural Science Foundation of China (No. U23A20495), National Key Research and Development Program of China (No. 2023YFC2509302), the Health Research and Innovation Capacity Enhancement Program of Shaanxi Province (2023 PT-10).

Disclosure

The authors report no conflicts of interest in this work.

References

1. Zhang H, Li H, Cao Z, Du J, Yan L, Wang J. Investigation of the in vivo integrity of polymeric micelles via large Stokes shift fluorophore-based FRET. *J Control Release*. 2020;324:47–54. doi:10.1016/j.jconrel.2020.04.046
2. Wang Q, Qin X, Fang J, Sun X. Nanomedicines for the treatment of rheumatoid arthritis: state of art and potential therapeutic strategies. *Acta Pharm Sin B*. 2021;11(5):1158–1174. doi:10.1016/j.apsb.2021.03.013
3. Ghezzi M, Pescina S, Padula C, et al. Polymeric micelles in drug delivery: an insight of the techniques for their characterization and assessment in biorelevant conditions. *J Control Release*. 2021;332:312–336. doi:10.1016/j.jconrel.2021.02.031
4. Sun X, Wang G, Zhang H, et al. The Blood Clearance Kinetics and Pathway of Polymeric Micelles in Cancer Drug Delivery. *ACS Nano*. 2018;12(6):6179–6192. doi:10.1021/acsnano.8b02830
5. Cai Y, Qi J, Lu Y, et al. The in vivo fate of polymeric micelles. *Adv Drug Deliv Rev*. 2022;188:114463. doi:10.1016/j.addr.2022.114463
6. Inoue Y, Takada K, Kawamura A, et al. Amphiphilic Liquid Crystalline Polymer Micelles That Exhibit a Phase Transition at Body Temperature. *ACS Appl Mater Interfaces*. 2022;14(28):31513–31524. doi:10.1021/acsami.2c00592
7. Jia N, Gao Y, Li M, et al. Metabolic reprogramming of proinflammatory macrophages by target delivered roburic acid effectively ameliorates rheumatoid arthritis symptoms. *Signal Transduct Target Ther*. 2023;8(1):280. doi:10.1038/s41392-023-01499-0
8. Zhang X, Gao X, Zhou J, et al. Albumin-based fluorescence resonance energy transfer nanoprobes for multileveled tumor tissue imaging and dye release imaging. *Colloids Surf B Biointerfaces*. 2021;199:111537. doi:10.1016/j.colsurfb.2020.111537
9. Pini F, Francés-Soriano L, Andrigo V, et al. Optimizing Upconversion Nanoparticles for FRET Biosensing. *ACS Nano*. 2023;17(5):4971–4984. doi:10.1021/acsnano.2c12523
10. Chen T, Li C, Li Y, et al. Small-Sized mPEG-PLGA Nanoparticles of Schisantherin A with Sustained Release for Enhanced Brain Uptake and Anti-Parkinsonian Activity. *ACS Appl Mater Interfaces*. 2017;9(11):9516–9527. doi:10.1021/acsami.7b01171
11. Hsiao F, Huang PY, Aoyagi T, Chang SF, Liaw J. In vitro and in vivo assessment of delivery of hydrophobic molecules and plasmid DNAs with PEO-PPO-PEO polymeric micelles on cornea. *J Food Drug Anal*. 2018;26(2):869–878. doi:10.1016/j.jfda.2017.09.002
12. Liu W, Li D, Dong Z, et al. Insight into the in vivo translocation of oral liposomes by fluorescence resonance energy transfer effect. *Int J Pharm*. 2020;587:119682. doi:10.1016/j.ijpharm.2020.119682
13. Chen T, He B, Tao J, et al. Application of Forster Resonance Energy Transfer (FRET) technique to elucidate intracellular and In Vivo biofate of nanomedicines. *Adv Drug Deliv Rev*. 2019;143:177–205. doi:10.1016/j.addr.2019.04.009
14. Parwani K, Patel F, Bhagwat P, et al. Swertiamarin mitigates nephropathy in high-fat diet/streptozotocin-induced diabetic rats by inhibiting the formation of advanced glycation end products. *Arch Physiol Biochem*. 2024;130(2):136–154. doi:10.1080/13813455.2021.1987478
15. Chang J, Zou S, Xiao Y, Zhu D. Identification and validation of targets of swertiamarin on idiopathic pulmonary fibrosis through bioinformatics and molecular docking-based approach. *BMC Complement Med Ther*. 2023;23(1):352. doi:10.1186/s12906-023-04171-w
16. Hairul-Islam MI, Saravanan S, Thirugnanasambantham K, et al. Swertiamarin, a natural steroid, prevent bone erosion by modulating RANKL/RANK/OPG signaling. *Int Immunopharmacol*. 2017;53:114–124. doi:10.1016/j.intimp.2017.10.022
17. Sharma M, Malim FM, Goswami A, et al. Neuroprotective Effect of Swertiamarin in a Rotenone Model of Parkinson's Disease: role of Neuroinflammation and Alpha-Synuclein Accumulation. *ACS Pharmacol Transl Sci*. 2023;6(1):40–51. doi:10.1021/acsptsci.2c00120
18. Zhao Z, He D, Wang J, et al. Swertiamarin relieves radiation-induced intestinal injury by limiting DNA damage. *mol Cell Biochem*. 2024;2024:1. doi:10.1007/s11010-024-05030-z
19. Nogales C, Mamdouh ZM, List M, Kiel C, Casas AI, Schmidt H. Network pharmacology: curing causal mechanisms instead of treating symptoms. *Trends Pharmacol Sci*. 2022;43(2):136–150. doi:10.1016/j.tips.2021.11.004
20. Talukdar S, Emdad L, Das SK, Fisher PB. EGFR: an essential receptor tyrosine kinase-regulator of cancer stem cells. *Adv Cancer Res*. 2020;147:161–188. doi:10.1016/bs.acr.2020.04.003
21. Chen N, Fan B, He Z, et al. Identification of HBEGF+ fibroblasts in the remission of rheumatoid arthritis by integrating single-cell RNA sequencing datasets and bulk RNA sequencing datasets. *Arthritis Res Ther*. 2022;24(1):215. doi:10.1186/s13075-022-02902-x
22. Jia N, Ma H, Zhang T, et al. Gentiopicroside attenuates collagen-induced arthritis in mice via modulating the CD147/p38/NF-kappaB pathway. *Int Immunopharmacol*. 2022;108:108854. doi:10.1016/j.intimp.2022.108854
23. Liu XR, Li SF, Mei WY, Liu XD, Zhou RB. Isorhamnetin Downregulates MMP2 and MMP9 to Inhibit Development of Rheumatoid Arthritis through SRC/ERK/CREB Pathway. *Chin J Integr Med*. 2024;30(4):299–310. doi:10.1007/s11655-023-3753-6
24. Sun J, Hu JR, Liu CF, et al. ANKRD49 promotes the metastasis of NSCLC via activating JNK-ATF2/c-Jun-MMP-2/9 axis. *BMC Cancer*. 2023;23(1):1108. doi:10.1186/s12885-023-11612-9
25. Yang YJ, Lu LJ, Wang JJ, et al. Tubson-2 decoction ameliorates rheumatoid arthritis complicated with osteoporosis in CIA rats involving isochlorogenic acid A regulating IL-17/MAPK pathway. *Phytomedicine*. 2023;116:154875. doi:10.1016/j.phymed.2023.154875
26. Zou P, Chen H, Paholak HJ, Sun D. Noninvasive fluorescence resonance energy transfer imaging of in vivo premature drug release from polymeric nanoparticles. *Mol Pharm*. 2013;10(11):4185–4194. doi:10.1021/mp4002393

27. Li M, Yang Y, Xiong L, Jiang P, Wang J, Li C. Metabolism, metabolites, and macrophages in cancer. *J Hematol Oncol*. 2023;16(1):80. doi:10.1186/s13045-023-01478-6
28. Weyand CM, Goronzy JJ. The immunology of rheumatoid arthritis. *Nat Immunol*. 2021;22(1):10–18. doi:10.1038/s41590-020-00816-x
29. Li Y, Liang Q, Zhou L, et al. An ROS-responsive artesunate prodrug nanosystem co- delivers dexamethasone for rheumatoid arthritis treatment through the HIF-1alpha/NF-kappaB cascade regulation of ROS scavenging and macrophage repolarization. *Acta Biomater*. 2022;152:406–424. doi:10.1016/j.actbio.2022.08.054
30. Fan D, Geng Q, Wang B, et al. Hypoxia-induced ALKBH5 aggravates synovial aggression and inflammation in rheumatoid arthritis by regulating the m6A modification of CH25H. *Clin Immunol Apr*. 2024;261:109929. doi:10.1016/j.clim.2024.109929
31. Wu H, Yuan H, Zhang J, et al. *Helicobacter pylori* upregulates PAD4 expression via stabilising HIF-1α to exacerbate rheumatoid arthritis. *Ann Rheum Dis*. 2024;83(12):1666–1676. doi:10.1136/ard-2023-225306
32. Li C, Li H, Wang Q, et al. pH-sensitive polymeric micelles for targeted delivery to inflamed joints. *J Control Release*. 2017;246:133–141. doi:10.1016/j.jconrel.2016.12.027
33. Vanderhaeghen T, Vandewalle J, Libert C. Hypoxia-inducible factors in metabolic reprogramming during sepsis. *FEBS J*. 2020;287(8):1478–1495. doi:10.1111/febs.15222
34. Karlsson J, Rhodes KR, Green JJ, Tzeng SY. Poly(beta-amino ester)s as gene delivery vehicles: challenges and opportunities. *Expert Opin Drug Deliv*. 2020;17(10):1395–1410. doi:10.1080/17425247.2020.1796628
35. Tao J, Wei Z, He Y, et al. Toward understanding the prolonged circulation and elimination mechanism of crosslinked polymeric micelles in zebrafish model. *Biomaterials*. 2020;256:120180. doi:10.1016/j.biomaterials.120180
36. Figus FA, Piga M, Azzolin I, McConnell R, Iagnocco A. Rheumatoid arthritis: extra-articular manifestations and comorbidities. *Autoimmun Rev*. 2021;20(4):102776. doi:10.1016/j.autrev.2021.102776
37. Norling LV, Headland SE, Dalli J, et al. Proresolving and cartilage-protective actions of resolvin D1 in inflammatory arthritis. *JCI Insight*. 2023;8(3):168728. doi:10.1172/jci.insight.168728
38. Deng C, Zhang Q, He P, et al. Targeted apoptosis of macrophages and osteoclasts in arthritic joints is effective against advanced inflammatory arthritis. *Nat Commun*. 2021;12(1):2174. doi:10.1038/s41467-021-22454-z
39. Faubert B, Solmonson A, DeBerardinis RJ. Metabolic reprogramming and cancer progression. *Science*. 2020;368(6487):5473. doi:10.1126/science.aaw5473
40. Weyand CM, Goronzy JJ. Immunometabolism in the development of rheumatoid arthritis. *Immunol Rev*. 2020;294(1):177–187. doi:10.1111/imr.12838
41. Tod MM, Padoin C, Petitjean O. Individualising aminoglycoside dosage regimens after therapeutic drug monitoring: simple or complex pharmacokinetic methods? *Clin Pharmacokinet*. 2001;40(11):803–814. doi:10.2165/00003088-200140110-00002
42. Cheng ML, Nakib D, Perciani CT, MacParland SA. The immune niche of the liver. *Clin Sci*. 2021;135(20):2445–2466. doi:10.1042/CS20190654
43. Li S, Shi J, Tang H. Animal models of drug-induced pulmonary fibrosis: an overview of molecular mechanisms and characteristics. *Cell Biol Toxicol*. 2022;38(5):699–723. doi:10.1007/s10565-021-09676-z
44. Zhang J, Zhao J, Ma Y, et al. Investigation of the Multi-Target Mechanism of Guanxin- Shutong Capsule in Cerebrovascular Diseases: a Systems Pharmacology and Experimental Assessment. *Front Pharmacol*. 2021;12:650770. doi:10.3389/fphar.2021.650770
45. Kehribar DY, Emmungil H, Turkmen NB, Ciftci O, Salva E, Ozgen M. EGFR blocker lapatinib inhibits the synthesis of matrix metalloproteinases from synovial fibroblasts. *Turk J Med Sci*. 2022;52(4):1355–1361. doi:10.55730/1300-0144.5442
46. Kanai T, Kondo N, Okada M, et al. The JNK pathway represents a novel target in the treatment of rheumatoid arthritis through the suppression of MMP-3. *J Orthop Surg Res*. 2020;15(1):87. doi:10.1186/s13018-020-01595-9
47. Zhao Z, Zhang Y, Wang C, Wang X, Wang Y, Zhang H. Angiotensin II upregulates RANKL/NFATC1 expression in synovial cells from patients with rheumatoid arthritis through the ERK1/2 and JNK pathways. *J Orthop Surg Res*. 2021;16(1):297. doi:10.1186/s13018-021-02451-0